Minimax Theory and its Applications
Volume 8 (2023), No. 1, 171–212

Truncated Hadamard-Babich Ansatz and Fast Huygens Sweeping Methods for Time-Harmonic Elastic Wave Equations in Inhomogeneous Media in the Asymptotic Regime

Jianliang Qian*, **Jian Song**
Department of Mathematics, Michigan State University, East Lansing, U.S.A.
qian@math.msu.edu, songji12@msu.edu

Wangtao Lu†
School of Mathematical Sciences, Zhejiang University, Hangzhou, Zhejiang, China
wangtaolu@zju.edu.cn

Robert Burridge
Dept. of Mathematics and Statistics, University of New Mexico, Albuquerque, U.S.A.
burridge137@gmail.com

Received: August 22, 2021
Accepted: November 18, 2021

In some applications, it is reasonable to assume that geodesics (rays) have a consistent orientation so that a time-harmonic elastic wave equation may be viewed as an evolution equation in one of the spatial directions. With such applications in mind, motivated by our recent work [*Hadamard-Babich ansatz for point-source elastic wave equations in variable media at high frequencies*, Multiscale Model Simul. 19/1 (2021) 46–86], we propose a new truncated Hadamard-Babich ansatz based globally valid asymptotic method, dubbed the fast Huygens sweeping method, for computing Green's functions of frequency-domain point-source elastic wave equations in inhomogeneous media in the high-frequency asymptotic regime and in the presence of caustics. The first novelty of the fast Huygens sweeping method is that the Huygens-Kirchhoff secondary-source principle is used to integrate many locally valid asymptotic solutions to yield a globally valid asymptotic solution so that caustics can be treated automatically. This yields uniformly accurate solutions both near the source and away from it. The second novelty is that a butterfly algorithm is adapted to accelerate matrix-vector products induced by the Huygens-Kirchhoff integral. The new method enjoys the following desired features: (1) it treats caustics automatically; (2) precomputed asymptotic ingredients can be used to construct Green's functions of elastic wave equations for many different point sources and for arbitrary frequencies; (3) given a specified number of points per wavelength, it constructs Green's functions in nearly optimal complexity $O(N \log N)$ in terms of the total number of mesh points N, where the prefactor of the complexity depends only on the specified accuracy and is independent of the frequency parameter. Three-dimensional numerical examples are presented to demonstrate the performance and accuracy of the new method.

Keywords: Hadamard-Babich ansatz, elastic wave, eikonal equation, fast Huygens sweeping, butterfly algorithm.

2010 Mathematics Subject Classification: 78A05, 78A46, 78M35.

* Partially supported by the National Science Foundation, grants 1614566 and 2012046.

† Partially supported by NSFC grant 12174310 and by the NSF of Zhejiang Province for distinguished young scholars LR21A010001.

ISSN 2199-1413 (printed), ISSN 2199-1421 (electronic) / $ 2.50

1. Introduction

We consider the following time-harmonic frequency-domain point-source elastic wave equation,

$$\begin{aligned}\rho\omega^2\boldsymbol{G} + (\lambda+\mu)\nabla(\nabla\cdot\boldsymbol{G}) + \mu\nabla^2\boldsymbol{G} + \nabla\lambda(\nabla\cdot\boldsymbol{G})\\ + \nabla\mu\times(\nabla\times\boldsymbol{G})) + 2(\nabla\mu\cdot\nabla)\boldsymbol{G} = -\boldsymbol{I}\delta(\boldsymbol{r}-\boldsymbol{r}_0),\end{aligned} \tag{1}$$

where the Kupradze-Sommerfeld radiation condition [16] is imposed at infinity, $\boldsymbol{G} = \boldsymbol{G}(\boldsymbol{r};\boldsymbol{r}_0)$ (with ω-dependence suppressed) is the so-called Green's tensor at the source $\boldsymbol{r}_0$, $\boldsymbol{I}$ is the 3×3 identity dyad, ω is the frequency parameter, $\rho(\boldsymbol{r})$ is the mass density, $\lambda(\boldsymbol{r})$ and $\mu(\boldsymbol{r})$ are the so-called Lamé's stiffness parameters, ∇ is the gradient operator, and $\boldsymbol{r} = (x_1, x_2, x_3)^T$. Since we are in the high-frequency regime, we assume that $\rho(\boldsymbol{r})$, $\lambda(\boldsymbol{r})$ and $\mu(\boldsymbol{r})$ are infinitely smooth and approach constants at infinity. When the frequency parameter ω is large, the solution of the elastic wave equation is highly oscillatory so that it is costly for direct methods such as finite-difference or finite-element methods to resolve these oscillations due to the so-called pollution or dispersion errors [4]. Therefore, alternative methods, such as geometrical optics (GO) based asymptotic methods, are sought to deal with such difficulties. In this paper, motivated by our recent work [34], we develop a new Hadamard-Babich (H-B) ansatz based globally valid asymptotic method, which we call the fast Huygens sweeping method, for the time-harmonic elastic wave equation in an inhomogeneous medium in the high frequency regime and in the presence of caustics.

Our new method consists of three critical components: a truncated H-B ansatz for computing locally valid asymptotic solutions, the Huygens-Kirchhoff secondary-source principle for integrating many local solutions into a global solution, and a butterfly algorithm for accelerating matrix-vector multiplication. We now motivate these three crucial elements.

Why we use the Hadamard-Babich ansatz

The following GO ansatz is usually used to expand the solution of the elastic wave equation (1),

$$\boldsymbol{G}(\boldsymbol{r};\boldsymbol{r}_0) = \sum_{l=0}^{\infty} \frac{\bar{\boldsymbol{A}}^l(\boldsymbol{r};\boldsymbol{r}_0)}{\omega^l} e^{i\omega\tau(\boldsymbol{r};\boldsymbol{r}_0)}, \tag{2}$$

where the unknowns $\bar{\boldsymbol{A}}^l$ and τ are independent of ω. The governing eikonal equations for τ and the transport equations for $\bar{\boldsymbol{A}}^l$ are derived in [15], but the corresponding initial conditions for $\bar{\boldsymbol{A}}^l$ are not specified since $\bar{\boldsymbol{A}}^l$ are singular at the source. Moreover, since the entire elastic wave in an isotropic medium as we consider here is composed of two wave modes, the compressional (P) wave and the shear (S) wave, and the S-wave mode is of some particular singularity at the point source [34], the common GO wisdom of keeping only the leading order term is not sufficient in terms of capturing the correct source singularity of the Green's tensor, which in turn will affect the overall accuracy of the asymptotic solution. Such an initialization difficulty at the point source also transpires in Helmholtz [2, 38] and Maxwell's equations [3, 22, 24, 32]. In a recent work [9], the Babich ansatz has been successfully used to remove the source singularity in a finite element method for the Helmholtz equation.

Consequently, in [34] we have developed the novel H-B ansatz for elastic wave equations to exactly resolve such an initialization difficulty at the source point. To achieve this purpose, we first apply the Hadamard's expansion in terms of the Gelfand-Shilov function [11] to the time-dependent elastic wave equation satisfied by the second-order time derivative of the Green's tensor. Since we can write out the explicit form of the second-order time derivative of the Green's tensor in a homogeneous elastic medium in terms of the Gelfand-Shilov function, we can derive the initial conditions of asymptotic ingredients by demanding that the generic Green's tensor match with the Green's tensor in a homogeneous medium at the source in an appropriate sense [34]. Once we have the time-domain Hadamard's ansatz available with appropriate initial conditions for asymptotic ingredients in place, we may take the Fourier transform in time of the time-domain ansatz to obtain the corresponding frequency-domain ansatz, yielding the desired Hadamard-Babich ansatz. Since this novel ansatz enables us to compute uniformly accurate asymptotic ingredients at the source, in [34] we have shown numerically that the new expansion indeed yields a uniformly accurate solution in a region containing the point source but no other caustics.

Why we use the Huygens principle

When we apply the GO ansatz (2) or the H-B ansatz to solve the elastic wave equation (1), we have implicitly assumed that the phase function τ is a single-valued, well-defined function in the sense that there is a unique ray connecting any observation point to the given source point. In fact, such an observation holds in general when applying the GO or H-B ansatz to solve other point-source wave equations. However, for waves propagating in an isotropic, generic inhomogeneous medium, there is a high probability that caustics may occur [42] so that some observation points may be connected to the given source point via multiple rays, making the phase function τ multivalued! Moreover, since the wavefield in the GO or H-B ansatz depends nonlinearly upon the phase function τ, we cannot simply add up multi-branched wavefields induced by the multivalued phase function. So what to do now? The Huygens principle comes to our rescue!

According to [1, 40], in an isotropic medium there always exists a small neighborhood of the source in which any observation point is connected to the source via a unique ray, so that the phase function τ is single-valued in this neighborhood; therefore, the GO or H-B ansatz is valid in this local neighborhood to yield a locally valid asymptotic solution. To go beyond caustics so as to account for multivalued phases implicitly, we use the Huygens secondary-source principle. Mathematically, to construct globally valid asymptotic solutions, we use the Huygens-Kirchhoff integral to integrate many locally valid asymptotic solutions in terms of waves rather than phases so that caustics are treated implicitly.

We sketch the methodology of using the Huygens secondary-source principle. To start with, we assume that geodesics (rays) have a consistent orientation so that elastic wave equations can be viewed as an evolution equation in one of the spatial directions. Hence, along this consistent orientation, we partition the computational domain into subdomains or layers satisfying certain properties and then develop a layer-by-layer sweeping solver to construct a globally valid primary-source Green's function by using the Huygens secondary-source principle. Specifically, we first choose as the first layer a neighborhood of the primary point source where the Green's function is locally valid. This can be achieved by locating a region where both the S- and P-wave phase functions are single-valued. Then we choose the boundary of this layer as the secondary-source surface and identify the second layer as the region where the asymptotic Green's functions excited by secondary sources are locally valid. Afterwards, the primary-source Green's function in the second layer can be computed by integrating those locally valid secondary-source Green's functions via the Huygens-Kirchhoff integral on the secondary-source surface. By repeating this process, we can sweep through the entire domain to construct the globally valid primary-source Green's function so that caustics are treated automatically and implicitly.

The question now is how to implement this sweeping strategy efficiently. To tackle this challenge, there are two major obstacles. The first obstacle is how to construct many locally valid secondary-source Green's functions rapidly, which boils down to how to rapidly construct corresponding asymptotic ingredients, such as phases and H-B expansion coefficients. To achieve this task, we propose to first compute phases and H-B expansion coefficients at each secondary source to higher order accuracy and then compress these functions or their relatives into low-rank separated representations in terms of tensor-product multivariate Chebyshev polynomials.

Computationally, since the information of each computed asymptotic ingredient is encoded into a small number of Chebyshev coefficients, such compression leads to significant storage reduction and efficient memory access.

Why we use the butterfly algorithm

The second obstacle is how to carry out efficiently dense matrix-vector multiplications induced by the discretized Huygens-Kirchhoff integral. To illustrate the point, we use the 3-D scalar Helmholtz equation as an example [23]. Let n be the number of mesh points along each coordinate direction of the computational domain, so that the total number of mesh points is $N = n^3$ in the 3-D case. Because we are interested in the globally valid asymptotic solution everywhere in the entire computational domain, the solution at observation points (receivers or nodes) corresponds to the result of some matrix-vector products. In the 3-D case, straightforward implementation of the above matrix-vector products will lead to $O(N^{\frac{2}{3}})$ operations for each receiver point, and the total computation cost will be $O(N^{\frac{5}{3}})$ as we need to carry out such matrix-vector products for roughly N points of receivers. Such computational cost is far too high to make our strategy practical.

Therefore, to tackle this difficulty, we adapt to our application the multilevel matrix decomposition based butterfly algorithm [7, 23, 26, 32, 33, 43]. The resulting butterfly algorithm allows us to carry out the required matrix-vector products with the total computational cost of $O(N \log N)$ complexity, where the prefactor depends only on the specified accuracy and is independent of the frequency parameter ω. Such low-rank rapid matrix-vector products are responsible for the adjective "fast" in the name "fast Huygens sweeping method" of our method.

Although the current work is motivated by [34], we emphasize that our new work presented in this article is different from [34] in several aspects: first, [34] only provides a locally valid asymptotic solution for the point-source elastic wave equation, while our current work constructs a globally valid asymptotic solution for the point-source elastic wave equation; second, the current work is based on [34] in the sense that it integrates many locally valid solution provided in [34] to obtain a globally valid asymptotic solution for the point-source problem by using the Huygens secondary-source principle (namely, the Huygens-Kirchhoff integral for elastic wave equations); third, our current work implements the Huygens-Kirchhoff numerical integration process rapidly by using the fast butterfly algorithm, and it is the first time that the fast butterfly algorithm is applied to solve the three-dimensional elastic wave equation to obtain a globally valid asymptotic solution.

Our fast Huygens sweeping method also has two unique merits which may be attributed to the precomputed tables of the asymptotic ingredients. The first merit is that because the asymptotic ingredients such as phase and H-B coefficients are independent of the frequency parameter, those tables can be used to construct asymptotic Green's functions at a given primary source for arbitrary frequencies. The second merit is that those tables can be used to construct asymptotic Green's functions at many other primary sources for arbitrary frequencies as well. These two merits are much desired in many applications, such as medical imaging and inverse problems.

1.1. Layout

The rest of the paper is organized as follows. In Section 2, we introduce the truncated H-B ansatz, a novel formulation to construct locally valid solutions of (1). In Section 3, we present details of computing asymptotic ingredients with desired order of accuracy. In Section 4, we present our fast Huygens sweeping method for constructing globally valid asymptotic Green's tensors as well as implementation details and complexity analysis. In Section 5, we show several numerical examples to illustrate the performance, effectiveness and accuracy of our method.

2. Hadamard-Babich ansatz for elastic waves

We are interested in the Green's tensor $\boldsymbol{G}(\boldsymbol{r};\boldsymbol{r}_0)$ for equation (1) at the primary source $\boldsymbol{r}_0$ in the high-frequency regime. In [34], by applying the Hadamard's expansion in the basis of the Gelfand-Shilov function to the time-domain elastic wave equation, we have obtained a novel asymptotic series based on spherical Hankel functions, dubbed the Hadamard-Babich ansatz, to expand the highly oscillatory Green's tensor for the frequency-domain elastic wave equation. This new ansatz yields uniform asymptotic solutions as the frequency parameter $\omega \to \infty$ in the region of space containing the point source but no other caustics.

We briefly summarize this novel construction. We apply the Hadamard's method to develop an asymptotic expansion to form the fundamental solution, starting from the following time-domain point-source elastic wave equation,

$$\begin{aligned}\rho\ddot{\boldsymbol{G}} - (\lambda+\mu)\nabla(\nabla\cdot\boldsymbol{G}) - \mu\nabla^2\boldsymbol{G} - \nabla\lambda(\nabla\cdot\boldsymbol{G})\\ - \nabla\mu\times(\nabla\times\boldsymbol{G})) - 2(\nabla\mu\cdot\nabla)\boldsymbol{G} = \boldsymbol{I}\delta(\boldsymbol{r}-\boldsymbol{r}_0)\delta(t),\end{aligned} \tag{3}$$

where $\boldsymbol{G} = \boldsymbol{G}(\boldsymbol{r},t;\boldsymbol{r}_0)$ indicating the dependence on time t.

According to [34], when parameters ρ, μ, and λ are constant, the second time-derivatives of the Green's tensors, $\ddot{\boldsymbol{G}}(\boldsymbol{r}, t; \boldsymbol{r}_0)$, take the following explicit forms for the two different wave modes,

$$\ddot{\boldsymbol{G}}^S_{hom} = \frac{\gamma^{S^3}}{\rho\pi}[2\gamma^{S^2} r^2 (\boldsymbol{I} - \tilde{\boldsymbol{r}}\tilde{\boldsymbol{r}}^T) f_+^{(-3)}(t^2 - \gamma^{S^2} r^2) - 2\boldsymbol{I} f_+^{(-2)}(t^2 - \gamma^{S^2} r^2)], \tag{4}$$

and
$$\ddot{\boldsymbol{G}}^P_{hom} = \frac{\gamma^{P^3}}{\rho\pi}\left[2\gamma^{P^3} r^2 \tilde{\boldsymbol{r}}\tilde{\boldsymbol{r}}^T f_+^{(-3)}(t^2 - \gamma^{P^2} r^2) - \boldsymbol{I} f_+^{(-2)}(t^2 - \gamma^{P^2} r^2)\right]. \tag{5}$$

Here $r = |\boldsymbol{r} - \boldsymbol{r}_0|$; the superscripts S and P refer to the S- and P-wave, respectively, and $\gamma^S = \sqrt{\frac{\rho}{\mu}}$ and $\gamma^P = \sqrt{\frac{\rho}{\lambda+2\mu}}$ are the S and P wave slowness (where these two slowness definitions are also valid for the non-constant case), respectively, as will become apparent later; the vector $\tilde{\boldsymbol{r}} = \frac{\boldsymbol{r}-\boldsymbol{r}_0}{|\boldsymbol{r}-\boldsymbol{r}_0|}$ is the unit tangent vector to the S- or P-ray as the case may be, and the S- and P-rays coincide in this special case of a uniform medium; the Gelfand-Shilov generalized function $f_+^{(k)}$ [11] is defined to be

$$f_+^{(k)}(x) = \frac{x_+^k}{k!} \text{ with } x_+ = \begin{cases} x & \text{for } x \geq 0, \\ 0 & \text{otherwise} \end{cases} \tag{6}$$

for $k > -1$; for other values of k, $f_+^{(k)}$ is defined by analytic continuation. Also, since

$$f_+^{(k)\prime} = f_+^{(k-1)}, \tag{7}$$

$f_+^{(k)}$ can be defined for negative integer values of k by successive differentiation in the sense of distribution. Since $f_+^{(0)}(x) = H(x)$, the Heaviside unit function, $f_+^{(-k-1)}(x) = \delta^{(k)}(x)$, the k-th derivative of the δ-function for $k = 0, 1, 2, \cdots$.

When the elastic parameters vary spatially in $\boldsymbol{r}$, the exact formulas of the Green's tensors are not available. However, the formulas (4) and (5) for the constant case motivate us to seek the solution of equation (3) in the following form of asymptotic series,

$$\ddot{\boldsymbol{G}}(\boldsymbol{r}, t; \boldsymbol{r}_0) = \sum_{l=0}^{\infty} \boldsymbol{A}^l(\boldsymbol{r}; \boldsymbol{r}_0) f_+^{(-3+l)}(t^2 - \mathcal{T}(\boldsymbol{r}; \boldsymbol{r}_0)), \tag{8}$$

where $\mathcal{T}(\boldsymbol{r}; \boldsymbol{r}_0) = \tau^2(\boldsymbol{r}; \boldsymbol{r}_0)$, and $\tau(\boldsymbol{r}; \boldsymbol{r}_0)$ is the traveltime from the source $\boldsymbol{r}_0$ to $\boldsymbol{r}$. We shall define $\boldsymbol{A}^l(\boldsymbol{r}; \boldsymbol{r}_0) \equiv 0$ for $l < 0$.

Plugging the asymptotic expansion (8) into the equation obtained from taking the double time-derivative of equation (3), we obtain two cases [34], and we call them Case I and Case II.

Case I, the S wave:

$$\nabla\mathcal{T} \cdot \boldsymbol{A}^0_j = 0, \text{ and } 4\rho\mathcal{T} - \mu|\nabla\mathcal{T}|^2 = 0, \tag{9}$$

or Case II, the P wave:

$$\boldsymbol{A}^0_j \parallel \nabla\mathcal{T}, \text{ and } 4\rho\mathcal{T} - (\lambda + 2\mu)|\nabla\mathcal{T}|^2 = 0, \tag{10}$$

where $\boldsymbol{A}^0_j$ is the jth column of $\boldsymbol{A}^0$.

In [34], we have derived the governing equations of traveltimes (a.k.a. phase functions) and amplitudes (a.k.a H-B coefficients) for both S- and P-waves, and we will show these equations for the truncated H-B ansatz later on.

Since $\boldsymbol{A}^l$ may not be smooth at the source for an inhomogeneous medium, we introduce $\tilde{\boldsymbol{A}}^l = \boldsymbol{A}^l\mathcal{T}^l$. Taking the Fourier transform of (8) in time, we can obtain the Green's function $\boldsymbol{G}$ for the frequency-domain point-source elastic wave equation known as the H-B ansatz,

$$\boldsymbol{G}(\boldsymbol{r};\boldsymbol{r}_0) = \sum_{l=0}^{\infty} \frac{\tilde{\boldsymbol{A}}^l(\boldsymbol{r};\boldsymbol{r}_0)}{-\omega^2\mathcal{T}^l(\boldsymbol{r};\boldsymbol{r}_0)} f_{-3+l+\frac{1}{2}}(\omega,\tau(\boldsymbol{r};\boldsymbol{r}_0)). \tag{11}$$

Here we have from [24]

$$f_\nu(\omega,\tau) := \int_\tau^\infty e^{i\omega t} f_+^{(\nu-\frac{1}{2})}(t^2-\tau^2(\boldsymbol{r};\boldsymbol{r}_0))dt = \frac{1}{2}i\sqrt{\pi}\left(\frac{2\tau}{\omega}\right)^\nu e^{i\omega\nu} H_\nu^{(1)}(\omega\tau), \tag{12}$$

where $H_\nu^{(1)}$ denotes the Hankel function of the first kind of order ν.

The governing equations and initial conditions for amplitudes $\tilde{\boldsymbol{A}}^l$ for both S- and P-waves are also derived in [34], and we will show these equations for the truncated H-B ansatz later on.

In order to distinguish the two wave modes, S-wave and P-wave, we introduce the following wave-mode specific Green's tensors,

$$\boldsymbol{G}^S(\boldsymbol{r};\boldsymbol{r}_0) = \sum_{l=0}^{\infty} \frac{\tilde{\boldsymbol{A}}^{Sl}(\boldsymbol{r};\boldsymbol{r}_0)}{-\omega^2\tau^{S2l}(\boldsymbol{r};\boldsymbol{r}_0)} f_{-3+l+\frac{1}{2}}(\omega,\tau^S(\boldsymbol{r};\boldsymbol{r}_0)), \tag{13}$$

where the superscript S refers to the S-wave, and

$$\boldsymbol{G}^P(\boldsymbol{r};\boldsymbol{r}_0) = \sum_{l=0}^{\infty} \frac{\tilde{\boldsymbol{A}}^{Pl}(\boldsymbol{r};\boldsymbol{r}_0)}{-\omega^2\tau^{P2l}(\boldsymbol{r};\boldsymbol{r}_0)} f_{-3+l+\frac{1}{2}}(\omega,\tau^P(\boldsymbol{r};\boldsymbol{r}_0)), \tag{14}$$

where the superscript P refers to the P wave. Since we are in the high-frequency regime and are dealing with a smooth elastic medium, we have

$$\boldsymbol{G}(\boldsymbol{r};\boldsymbol{r}_0) = \boldsymbol{G}^S(\boldsymbol{r};\boldsymbol{r}_0) + \boldsymbol{G}^P(\boldsymbol{r};\boldsymbol{r}_0). \tag{15}$$

3. Numerics for the truncated H-B ansatz

3.1. Truncating the ansatz for the S-wave

Since, numerically, it is impossible to construct $\tilde{\boldsymbol{A}}^{Sl}$ for all $l \geq 0$, we need to truncate the ansatz in implementation. In order to at least reproduce the fundamental solution (4) in a homogeneous medium, we truncate the formula (13) to keep only two terms,

$$\boldsymbol{G}^S(\boldsymbol{r};\boldsymbol{r}_0) = \frac{\tilde{\boldsymbol{A}}^{S0}(\boldsymbol{r};\boldsymbol{r}_0)}{-\omega^2} f_{-3+\frac{1}{2}}(\omega,\tau^S(\boldsymbol{r};\boldsymbol{r}_0)) + \frac{\tilde{\boldsymbol{A}}^{S1}(\boldsymbol{r};\boldsymbol{r}_0)}{-\omega^2\mathcal{T}(\boldsymbol{r};\boldsymbol{r}_0)} f_{-2+\frac{1}{2}}(\omega,\tau^S(\boldsymbol{r};\boldsymbol{r}_0)), \tag{16}$$

where the superscript S refers to the S-wave and $\mathcal{T} = {\tau^S}^2$.

In [34] we have verified that keeping the first two terms is sufficient to capture the S-wave source singularity. Here we summarize the governing equations for τ^S, $\tilde{\boldsymbol{A}}^{S0}$ and $\tilde{\boldsymbol{A}}^{S1}$ for the S-wave as the following [34].

We have the eikonal equation for τ^S,

$$|\nabla\tau^S| = \gamma^S \tag{17}$$

with the initial condition $\tau^S(\boldsymbol{r}_0;\boldsymbol{r}_0) = 0$, where γ^S is the S-wave slowness function, $\gamma^S = \sqrt{\frac{\rho}{\mu}}$, and $\mathcal{T} = {\tau^S}^2$.

We have the transport equation for the leading H-B coefficient $\tilde{\boldsymbol{A}}^{S0}$,

$$(\nabla\mathcal{T}\cdot\nabla)\tilde{\boldsymbol{A}}^{S0} + \frac{1}{2\mu}[\nabla\cdot(\mu\nabla\mathcal{T}) - 14\rho]\tilde{\boldsymbol{A}}^{S0} + \frac{\mu}{2\rho}\nabla\mathcal{T}\left[\nabla\left(\frac{\rho}{\mu}\right)\cdot\tilde{\boldsymbol{A}}^{S0}\right] = 0, \tag{18}$$

with the initial condition

$$\tilde{\boldsymbol{A}}^{S0} = \frac{\mathcal{T}^{\frac{5}{2}}}{\rho_0\pi r^3}(\boldsymbol{I} - 3\tilde{\boldsymbol{r}}\tilde{\boldsymbol{r}}^T) + \frac{{\gamma_0^S}^2\mathcal{T}^{\frac{3}{2}}}{\rho_0\pi r}(\boldsymbol{I} + \tilde{\boldsymbol{r}}\tilde{\boldsymbol{r}}^T) + O(\mathcal{T}^{\frac{3}{2}}), \tag{19}$$

where $\gamma_0^S = \gamma^S(\boldsymbol{r}_0)$ and $\rho_0 = \rho(\boldsymbol{r}_0)$.

We have the transport equation for the second H-B coefficient $\tilde{\boldsymbol{A}}^{S1}$,

$$(\nabla\mathcal{T}\cdot\nabla)\tilde{\boldsymbol{A}}^{S1} + \frac{1}{2\mu}[\nabla\cdot(\mu\nabla\mathcal{T}) - 18\rho]\tilde{\boldsymbol{A}}^{S1} + \frac{\mu}{2\rho}\nabla\mathcal{T}\left[\nabla\left(\frac{\rho}{\mu}\right)\cdot\tilde{\boldsymbol{A}}^{S1}\right] = \tilde{\boldsymbol{R}}^0,$$

where

$$\tilde{\boldsymbol{R}}^0 = -\frac{\nabla\mathcal{T}\tilde{\boldsymbol{a}}^0}{2} + \frac{\mu\nabla\mathcal{T}[(\nabla\mathcal{T}\cdot\nabla)\tilde{\boldsymbol{a}}^0]}{4\rho} - \frac{\nabla\mathcal{T}\tilde{\boldsymbol{b}}^0}{8\rho} \tag{20}$$

$$-\frac{\mathcal{T}\nabla\lambda\tilde{\boldsymbol{a}}^0}{2\mu} - \frac{(\lambda+\mu)\mathcal{T}\nabla\tilde{\boldsymbol{a}}^0}{2\mu} + \frac{\mathcal{T}\tilde{\boldsymbol{B}}^0}{2\mu}. \tag{21}$$

Here $\tilde{\boldsymbol{B}}^0$, the row vector $\tilde{\boldsymbol{a}}^0$, and the row vector $\tilde{\boldsymbol{b}}^0$ are given by

$$\begin{aligned}\tilde{\boldsymbol{B}}^0 &= (\lambda+\mu)\nabla(\nabla\cdot\tilde{\boldsymbol{A}}^{S0}) + \mu\nabla^2\tilde{\boldsymbol{A}}^{S0} + \nabla\lambda(\nabla\cdot\tilde{\boldsymbol{A}}^{S0})\\ &\quad + \nabla\mu\times(\nabla\times\tilde{\boldsymbol{A}}^{S0}) + 2(\nabla\mu\cdot\nabla)\tilde{\boldsymbol{A}}^{S0}, \qquad (22)\\ \tilde{\boldsymbol{a}}^0 &= \nabla\cdot\tilde{\boldsymbol{A}}^{S0} + \frac{1}{\lambda+\mu}\nabla\mu\cdot\tilde{\boldsymbol{A}}^{S0} + \frac{2\mu}{(\lambda+\mu)|\nabla\mathcal{T}|^2}\nabla\mathcal{T}[(\nabla\mathcal{T}\cdot\nabla)\tilde{\boldsymbol{A}}^{S0}], \qquad (23)\\ \tilde{\boldsymbol{b}}^0 &= 10\rho\tilde{\boldsymbol{a}}^0 - (\lambda+\mu)(\nabla\mathcal{T}\cdot\nabla)\tilde{\boldsymbol{a}}^0 - \mu\nabla^2\mathcal{T}\tilde{\boldsymbol{a}}^0\\ &\quad - (\nabla\mathcal{T}\cdot\nabla\lambda)\tilde{\boldsymbol{a}}^0 - (\nabla\mathcal{T}\cdot\nabla\mu)\tilde{\boldsymbol{a}}^0 + \nabla\mathcal{T}\cdot\tilde{\boldsymbol{B}}^0. \qquad (24)\end{aligned}$$

And the initial condition for $\tilde{\boldsymbol{A}}^{S1}$ is

$$\tilde{\boldsymbol{A}}^{S1} = -\frac{3}{2}\tilde{\boldsymbol{A}}^{S0} + \frac{\mathcal{T}^{\frac{5}{2}}}{\rho_0\pi r^3}(\boldsymbol{I} - 3\tilde{\boldsymbol{r}}\tilde{\boldsymbol{r}}^T) + O(\mathcal{T}^2). \tag{25}$$

Because these governing equations are weakly coupled to each other, we need to design appropriate schemes to solve these equations up to suitable orders of accuracy. To obtain a first-order accurate approximation of $\tilde{\boldsymbol{A}}^{S1}$ by solving the corresponding transport equation, we need a third-order accurate approximation of $\tilde{\boldsymbol{A}}^{S0}$, since equation (3.1) involves the second-order derivative of $\tilde{\boldsymbol{A}}^{S0}$ in its right-hand side. Moreover, a third-order accurate $\tilde{\boldsymbol{A}}^{S0}$ requires a fifth-order accurate τ^S due to the appearance of $\Delta\mathcal{T}$ in (18). For the eikonal equation (17), we can employ Lax-Friedrichs (LxF) high-order weighted essentially non-oscillatory (WENO) based schemes developed in [12, 13, 14, 20, 21, 30, 38, 39, 45, 46]. Since the governing equations for $\tilde{\boldsymbol{A}}^{S0}$ and $\tilde{\boldsymbol{A}}^{S1}$ are linear, we can also apply LxF-WENO based schemes directly to the linear system. But since the S-wave is analogous to the electromagnetic wave satisfying the Maxwell's equations, we employ the schemes developed in [22] to decouple the components of $\tilde{\boldsymbol{A}}^{S0}$. Namely, instead of computing the nine components of $\tilde{\boldsymbol{A}}^{S0}$ directly, we decouple the governing transport equation so that we are able to compute $\tilde{\boldsymbol{A}}^{S0}$ more efficiently.

We mention in passing that one essential difficulty in solving point-source eikonal and transport equations to high-order accuracy is how to properly treat the upwind singularity of the eikonal equation at the point source. To do that, one may use an adaptive mesh refinement method at the source [35] or use either multiplicative or additive factorization of singularity at the source [10, 25, 27, 31, 44].

3.1.1. Computing take-off directions

In our computational algorithm, we frequently need to use the so-called take-off direction, and we derive the related transport equation for computing this quantity.

Suppose that $\mathcal{T} = \tau^{S^2}$ is available. According to the method of characteristics, a geodesic ray tracing out from $\boldsymbol{r}_0$ to $\boldsymbol{r}$ is governed by

$$\boldsymbol{t}^{(1)}(\boldsymbol{r};\boldsymbol{r}_0) := \dot{\boldsymbol{r}} = \frac{d\boldsymbol{r}}{ds} = \frac{\nabla\tau^S(\boldsymbol{r}(s))}{\gamma^S}, \tag{26}$$

where the s parameter is the arc length parameter and the $\dot{}$ indicates the derivative in s. The unit take-off vector at a given spatial position $\boldsymbol{r}$ is defined as

$$\boldsymbol{t}^{(0)}(\boldsymbol{r};\boldsymbol{r}_0) := \lim_{\boldsymbol{r}'\to\boldsymbol{r}_0} \boldsymbol{t}^{(1)}(\boldsymbol{r}';\boldsymbol{r}_0), \tag{27}$$

where $\boldsymbol{r}'$ approaches $\boldsymbol{r}_0$ along the geodesic ray from $\boldsymbol{r}_0$ to $\boldsymbol{r}$. It is clear that $\boldsymbol{t}^{(0)}$ is invariant along each geodesic ray so that it is governed by the following advection equation,

$$\dot{\boldsymbol{t}}^{(0)}(\boldsymbol{r};\boldsymbol{r}_0) = \frac{\nabla\tau^S\cdot\nabla}{\gamma^S}\boldsymbol{t}^{(0)} = \boldsymbol{0}, \tag{28}$$

with the initial condition
$$\lim_{\boldsymbol{r}\to\boldsymbol{r}_0}\left(\boldsymbol{t}^{(0)}(\boldsymbol{r};\boldsymbol{r}_0) - \tilde{\boldsymbol{r}}\right) = 0, \tag{29}$$

where $\tilde{\boldsymbol{r}} = \frac{\boldsymbol{r}-\boldsymbol{r}_0}{|\boldsymbol{r}-\boldsymbol{r}_0|}$.

3.1.2. Computing $\tilde{\boldsymbol{A}}^{S0}$

Following [22], we first write $\tilde{\boldsymbol{A}}^{S0} = A\boldsymbol{P}^{(1)}$, where A is a scalar amplitude function and $\boldsymbol{P}^{(1)} = (\boldsymbol{P}_1^{(1)}, \boldsymbol{P}_2^{(1)}, \boldsymbol{P}_3^{(1)})$ is the 3 by 3 polarization dyad, and we then insert this into equation (18) to obtain

$$(\nabla\mathcal{T}\cdot\nabla A)\boldsymbol{P}^{(1)} + A(\nabla\mathcal{T}\cdot\nabla)\boldsymbol{P}^{(1)} + A\frac{1}{2\mu}[\nabla\cdot(\mu\nabla\mathcal{T}) - 14\rho]\boldsymbol{P}^{(1)} + \frac{\mu}{2\rho}A\nabla\mathcal{T}\left[\nabla\left(\frac{\rho}{\mu}\right)\cdot\boldsymbol{P}^{(1)}\right] = 0. \tag{30}$$

By property of the S-wave, we know that $\nabla\mathcal{T}$ is orthogonal to the two-dimensional subspace spanned by the columns of $\boldsymbol{P}^{(1)}$, and we further assume that the norm of the polarization vector $\boldsymbol{P}_j^{(1)}$, $1 \le j \le 3$, is invariant along a ray $\boldsymbol{r}(s)$; consequently, $\frac{d}{ds}\boldsymbol{P}_j^{(1)}\cdot\boldsymbol{P}_j^{(1)} = 0$ so that we have

$$\boldsymbol{P}_j^{(1)}\cdot(\nabla\mathcal{T}\cdot\nabla)\boldsymbol{P}_j^{(1)} = 0, \tag{31}$$

where we have used the property that $\frac{d}{ds} = \nabla\mathcal{T}\cdot\nabla$ along a ray with s the arc length parameter. Taking the dot product of equation (30) with $\boldsymbol{P}_j^{(1)}$ in terms of individual columns, we can obtain

$$\nabla\mathcal{T}\cdot\nabla A + \frac{1}{2\mu}[\nabla\cdot(\mu\nabla\mathcal{T}) - 14\rho]A = 0. \tag{32}$$

Inserting equation (32) into equation (30), we get the following equation for $\boldsymbol{P}_j^{(1)}$:

$$(\nabla\mathcal{T}\cdot\nabla)\boldsymbol{P}_j^{(1)} + \frac{\mu}{2\rho}\nabla\mathcal{T}\left[\nabla\left(\frac{\rho}{\mu}\right)\cdot\boldsymbol{P}_j^{(1)}\right] = 0, \tag{33}$$

so that we see that $\frac{d}{ds}\boldsymbol{P}_j^{(1)}$ is parallel to $\nabla\mathcal{T}$. The above decomposition is analogous to that in [22] which introduces a variable v_0 satisfying that $\tilde{\boldsymbol{A}}^{S0} = v_0\mathcal{T}\boldsymbol{P}^{(1)}$.

Since, in a small neighborhood of the primary source $\boldsymbol{r}_0$, $\gamma^S(\boldsymbol{r})$ and $\rho(\boldsymbol{r})$ approximately equal γ_0^S and ρ_0, respectively, we expect that $\tilde{\boldsymbol{A}}^{S0}$ is consistent with

$$\frac{2{\gamma_0^S}^5|\boldsymbol{r}-\boldsymbol{r}_0|^2}{\rho_0\pi}(\boldsymbol{I} - \tilde{\boldsymbol{r}}\tilde{\boldsymbol{r}}^T)$$

in this neighborhood according to the S-wave Green's tensor (4). Therefore, we enforce the following initial conditions

$$\lim_{\boldsymbol{r}\to\boldsymbol{r}_0}\left(A(\boldsymbol{r};\boldsymbol{r}_0) - \frac{2{\gamma_0^S}^5|\boldsymbol{r}-\boldsymbol{r}_0|^2}{\rho_0\pi}\right) = 0, \tag{34}$$

$$\lim_{\boldsymbol{r}\to\boldsymbol{r}_0}\left(\boldsymbol{P}^{(1)}(\boldsymbol{r};\boldsymbol{r}_0) - (\boldsymbol{I} - \tilde{\boldsymbol{r}}\tilde{\boldsymbol{r}}^T)\right) = 0, \tag{35}$$

where the limit $\boldsymbol{r}\to\boldsymbol{r}_0$ should be understood in the sense that $\boldsymbol{r}$ approaches $\boldsymbol{r}_0$ along its ray $\boldsymbol{r}(s)$ as $s\to 0^+$.

Now by writing $A = v_0\mathcal{T}$, we can derive the governing equation for v_0,

$$\nabla\mathcal{T}\cdot\nabla v_0 + \frac{1}{2\mu}[\nabla\cdot(\mu\nabla\mathcal{T}) - 6\rho]v_0 = 0, \tag{36}$$

with the initial condition $v_0(\boldsymbol{r};\boldsymbol{r}_0) = \frac{2\gamma_0^{S^3}}{\rho_0\pi}$. Following [22], the above transport equation has the following solution along the unique ray connecting $\boldsymbol{r}$ and $\boldsymbol{r}_0$,

$$v_0(\tau^S) = \frac{2\gamma_0^{S^3}}{\rho_0\pi}\exp\left(-\int_0^{\tau^S}\frac{\nabla\cdot(\mu\nabla\tau'^2) - 6\rho}{4\tau'\mu\gamma^{S^2}}d\tau'\right). \tag{37}$$

If we define $\boldsymbol{P}^{(0)} = \left(\boldsymbol{I} - \boldsymbol{t}^{(0)}\boldsymbol{t}^{(0)^T}\right)$, then we can derive the following relations by using equation (28),

$$\dot{\boldsymbol{P}}^{(0)} = 0, \tag{38}$$

$$\boldsymbol{t}^{(0)}\cdot\boldsymbol{P}^{(0)} = 0, \tag{39}$$

with the initial condition

$$\boldsymbol{P}^{(0)}(\boldsymbol{r};\boldsymbol{r}_0) - (\boldsymbol{I} - \tilde{\boldsymbol{r}}\tilde{\boldsymbol{r}}^T) = O(r) \quad \text{as} \quad \boldsymbol{r}\to\boldsymbol{r}_0 \tag{40}$$

due to equation (29).

We may use the method proposed in [22] to compute A and $\boldsymbol{P}^{(1)}$ with desired order of accuracy. In comparison with the method of applying the LxF WENO-based schemes directly to the governing equations (18), the method in [22] is more efficient in computing nine components of $\tilde{\boldsymbol{A}}^{S0}$, and we therefore adopt this method in our implementation; we omit the related details here.

3.1.3. Computing $\tilde{\boldsymbol{A}}^{S1}$

We first notice that, in equation (3.1), the term $\nabla\mathcal{T}(\nabla(\frac{\rho}{\mu})\cdot\tilde{\boldsymbol{A}}^{S1})$ entangles with $\tilde{\boldsymbol{A}}^{S1}$. Since we know that $\tilde{\boldsymbol{A}}_j^{S0}$, $1\le j\le 3$, are orthogonal to $\nabla\mathcal{T}$, we take the scalar product of equation (3.1) columnwise with $\tilde{\boldsymbol{A}}_j^{S0}$ so that we can obtain a decoupled governing equation. Thus, we have

$$\begin{aligned}&(\nabla\mathcal{T}\cdot\nabla)g_{kj} + \frac{1}{\mu}[\nabla\cdot(\mu\nabla\mathcal{T}) - 16\rho]g_{kj} \\ &\quad= \tilde{\boldsymbol{R}}_k^0\cdot\tilde{\boldsymbol{A}}_j^{S0} - \frac{\mu}{2\rho}\mathcal{T}\left(\nabla\left(\frac{\rho}{\mu}\right)\cdot\tilde{\boldsymbol{A}}_j^{S0}\right)\left(\nabla\cdot\tilde{\boldsymbol{A}}_k^{S0} - \frac{\mu^3}{\rho(\lambda+\mu)}\nabla\left(\frac{\rho}{\mu^2}\right)\cdot\tilde{\boldsymbol{A}}_k^{S0}\right),\end{aligned} \tag{41}$$

where $g_{kj} = \tilde{\boldsymbol{A}}_k^{S1}\cdot\tilde{\boldsymbol{A}}_j^{S0}$, and we have used the relation [34]

$$\nabla\mathcal{T}\cdot\tilde{\boldsymbol{A}}_k^{S1} = \mathcal{T}\nabla\cdot\tilde{\boldsymbol{A}}_k^{S0} - \frac{\mu^3\mathcal{T}}{\rho(\lambda+\mu)}\nabla\left(\frac{\rho}{\mu^2}\right)\cdot\tilde{\boldsymbol{A}}_k^{S0}. \tag{42}$$

Since $\tilde{\boldsymbol{A}}^{S0} = O(r^2)$ and $\tilde{\boldsymbol{A}}^{S1} = O(r^2)$, $g_{kj} = O(r^4)$ are very close to 0 near $\boldsymbol{r}_0$, making numerical errors quite sensitive to the initialization and inducing numerical instabilities.

To remedy the situation, we define new variables

$$\tilde{g}_{kj} := g_{kl}/\mathcal{T}. \tag{43}$$

Hence we get the following governing equations

$$\begin{aligned}&(\nabla\mathcal{T}\cdot\nabla)\tilde{g}_{kj} + \frac{1}{\mu}[\nabla\cdot(\mu\nabla\mathcal{T}) - 12\rho]\tilde{g}_{kj}\\ &= \frac{\tilde{\boldsymbol{R}}_k^0\cdot\tilde{\boldsymbol{A}}_j^{S0}}{\mathcal{T}} - \frac{\mu}{2\rho}\left(\nabla\left(\frac{\rho}{\mu}\right)\cdot\tilde{\boldsymbol{A}}_j^{S0}\right)\left(\nabla\cdot\tilde{\boldsymbol{A}}_k^{S0} - \frac{\mu^3}{\rho(\lambda+\mu)}\nabla\left(\frac{\rho}{\mu^2}\right)\cdot\tilde{\boldsymbol{A}}_k^{S0}\right),\end{aligned} \tag{44}$$

with the initial condition $$\tilde{g}_{kj} = -\frac{4\gamma_0^{S^8} r^2}{\rho_0^2\pi^2}(\boldsymbol{I} - \tilde{\boldsymbol{r}}\tilde{\boldsymbol{r}}^T)_{kj}. \tag{45}$$

Then the LxF WENO-based schemes can be used to compute $\tilde{g}_{kj}$. Once all $\tilde{g}_{kj}$ are available, we can obtain the dyadic coefficients $\tilde{\boldsymbol{A}}^{S1}$ by using the method proposed in [22] and details are omitted here.

3.2. Truncating the ansatz for the P-wave

We truncate formula (14) to keep only two terms,

$$\begin{aligned}&\boldsymbol{G}^P(\boldsymbol{r};\boldsymbol{r}_0)\\ &= \frac{\tilde{\boldsymbol{A}}^{P0}(\boldsymbol{r};\boldsymbol{r}_0)}{-\omega^2} f_{-3+\frac{1}{2}}(\omega, \tau^P(\boldsymbol{r};\boldsymbol{r}_0)) + \frac{\tilde{\boldsymbol{A}}^{P1}(\boldsymbol{r};\boldsymbol{r}_0)}{-\omega^2\mathcal{T}(\boldsymbol{r};\boldsymbol{r}_0)} f_{-2+\frac{1}{2}}(\omega, \tau^P(\boldsymbol{r};\boldsymbol{r}_0)),\end{aligned} \tag{46}$$

where the superscript P refers to the P-wave and $\mathcal{T} = \tau^{P^2}$.

We have the following eikonal equation for the P-wave,

$$|\nabla\tau^P| = \gamma^P, \tag{47}$$

with the initial condition $\tau^P(\boldsymbol{r}_0;\boldsymbol{r}_0) = 0$, where $\gamma^P = \sqrt{\frac{\rho}{\lambda+2\mu}}$.

For the P-wave we have the following relation for $\tilde{\boldsymbol{A}}^{P0}$ and $\tilde{\boldsymbol{A}}^{P1}$ [34],

$$\tilde{\boldsymbol{A}}^{P0} = \nabla\mathcal{T}\tilde{\boldsymbol{\alpha}}^0, \tag{48}$$

$$\tilde{\boldsymbol{A}}^{P1} = \tilde{\boldsymbol{C}}^0 + \nabla\mathcal{T}\tilde{\boldsymbol{\alpha}}^1, \tag{49}$$

where $\tilde{\boldsymbol{\alpha}}^0 = (\tilde{\alpha}_1^0, \tilde{\alpha}_2^0, \tilde{\alpha}_3^0)$ and $\tilde{\boldsymbol{\alpha}}^1 = (\tilde{\alpha}_1^1, \tilde{\alpha}_2^1, \tilde{\alpha}_3^1)$ are row vectors, which are governed by some transport equations. According to [34], the governing equations for $\tilde{\boldsymbol{\alpha}}^0$ are

$$\nabla\mathcal{T}\cdot\nabla\tilde{\boldsymbol{\alpha}}^0 + [\frac{1}{2\rho}\nabla\cdot(\rho\nabla\mathcal{T}) - \frac{5\rho}{\lambda+2\mu}]\tilde{\boldsymbol{\alpha}}^0 = 0, \tag{50}$$

with the initial condition

$$\tilde{\boldsymbol{\alpha}}^0 = \frac{\gamma_0^{P^3}}{\rho_0\pi}(\boldsymbol{r} - \boldsymbol{r}_0) + O(r^2) \quad \text{as} \quad \boldsymbol{r}\to\boldsymbol{r}_0. \tag{51}$$

Similarly, according to [34], the governing equations for $\tilde{\boldsymbol{\alpha}}^1$ are

$$\nabla\mathcal{T}\cdot\nabla\tilde{\boldsymbol{\alpha}}^1 + [\frac{1}{2\rho}\nabla\cdot(\rho\nabla\mathcal{T}) - \frac{7\rho}{\lambda+2\mu}]\tilde{\boldsymbol{\alpha}}^1 = \tilde{\boldsymbol{c}}^0, \tag{52}$$

with the initial condition $\tilde{\boldsymbol{\alpha}}^0 = O(r^2)$ as $\boldsymbol{r} \to \boldsymbol{r}_0$, where $\tilde{\boldsymbol{c}}^0$ is

$$\begin{aligned}\tilde{\boldsymbol{c}}^0 = \frac{1}{8\rho}\{10\rho - \mu\nabla^2\mathcal{T} - \nabla\mathcal{T}\cdot\nabla(\lambda+\mu)](\nabla\mathcal{T}\cdot\tilde{\boldsymbol{C}}^0) - (\lambda+\mu)\nabla\mathcal{T}\cdot\nabla(\nabla\mathcal{T}\cdot\tilde{\boldsymbol{C}}^0) \\ - (\lambda+\mu)|\nabla\mathcal{T}|^2(\nabla\cdot\tilde{\boldsymbol{C}}^0) - 2\mu\nabla\mathcal{T}\cdot[(\nabla\mathcal{T}\cdot\nabla)\tilde{\boldsymbol{C}}^0] - (\nabla\mu\cdot\tilde{\boldsymbol{C}}^0)|\nabla\mathcal{T}|^2 + \tilde{\boldsymbol{d}}^0\}. \quad (53)\end{aligned}$$

Here $\tilde{\boldsymbol{C}}^0$ and $\tilde{\boldsymbol{d}}^0$ are defined to be

$$\tilde{\boldsymbol{C}}^0 \equiv -\nabla\tilde{\boldsymbol{\alpha}}^0 - \frac{(\lambda+2\mu)^2}{\rho(\lambda+\mu)}\nabla\left(\frac{\rho}{\lambda+2\mu}\right)\tilde{\boldsymbol{\alpha}}^0 - \frac{\nabla\lambda\tilde{\boldsymbol{\alpha}}^0}{\lambda+\mu}, \quad (54)$$

$$\begin{aligned}\tilde{\boldsymbol{d}}^0 \equiv (\lambda+\mu)\nabla\mathcal{T}\cdot\nabla(\nabla\cdot\tilde{\boldsymbol{A}}^{P0}) + \mu\nabla\mathcal{T}\cdot\nabla^2\tilde{\boldsymbol{A}}^{P0} + (\nabla\lambda\cdot\nabla\mathcal{T})(\nabla\cdot\tilde{\boldsymbol{A}}^{P0}) \\ + \nabla\mathcal{T}\cdot[\nabla\mu\times(\nabla\times\tilde{\boldsymbol{A}}^{P0})] + 2\nabla\mathcal{T}\cdot[(\nabla\mu\cdot\nabla)\tilde{\boldsymbol{A}}^{P0}]. \quad (55)\end{aligned}$$

To compute the formula (46) numerically, we need to solve the eikonal equation (47) to obtain τ^P, and the governing equations (50) and (52) to obtain $\tilde{\boldsymbol{A}}^{P0}$ and $\tilde{\boldsymbol{A}}^{P1}$, respectively. To obtain a first-order accurate $\boldsymbol{G}^P$, we need a fifth-order accurate τ^P, a third-order accurate $\tilde{\boldsymbol{\alpha}}^0$, and a first-order accurate $\tilde{\boldsymbol{\alpha}}^1$. For the eikonal equation (47), we can employ fifth-order LxF WENO-based schemes developed in [38] to compute τ^P. Since the governing equations (50) and (52) are decoupled, we can also apply high-order schemes in [38] to compute $\tilde{\boldsymbol{\alpha}}^0$ and $\tilde{\boldsymbol{\alpha}}^1$ with desired oder of accuracy.

4. Huygens principle based globally valid Green's functions

As motivated in the Introduction and verified in [34], the truncated H-B ansatz provides an approximation to the Green's tensor if no caustic occurs in the region of space containing the point source, and the resulting Green's tensor is locally valid and does not contain the interference effect due to multivaluedness of phase functions. As motivated in the introduction, to get back such interference effects, we will use the Huygens principle to integrate many locally valid H-B Green's tensors so that we can construct a globally valid Green's tensor in a coherent way, and the Huygens-Kirchhoff formula for elastic wave fields is exactly the vehicle that we need.

We mention in passing that in the setting of time-dependent Schrodinger or wave equations, the Huygens principle has been used *implicitly* to reinitialize Gaussian beam propagation in [18, 36, 37] and *explicitly* to restart wave propagation in [17, 19].

4.1. Huygens-Kirchhoff formula for elastic wave fields

Assuming that the wave field $\boldsymbol{u}(\boldsymbol{r};\boldsymbol{r}_0)$ due to the primary source $\boldsymbol{r}_0$ is known for $\boldsymbol{r}\in\Omega$ in a domain Ω enclosing the primary source $\boldsymbol{r_0}$, we would like to extrapolate this wave field to obtain the wave field $\boldsymbol{u}(\boldsymbol{r};\boldsymbol{r}_0)$ for $\boldsymbol{r}\in\Omega_{\text{ext}}$ in the exterior domain Ω_{ext}; see Figure 4.1.

As illustrated in Figure 4.1, the elastic wave field $\boldsymbol{u}(\boldsymbol{r};\boldsymbol{r}_0)$ in Ω_{ext} excited by the source $\boldsymbol{r}_0$ satisfies the following equation,

$$\begin{aligned}\rho(\boldsymbol{r})\omega^2 u_k(\boldsymbol{r};\boldsymbol{r}_0) + \partial_j\big[\lambda(\boldsymbol{r})\delta_{kj}\partial_m u_m(\boldsymbol{r};\boldsymbol{r}_0) \\ + \mu(\partial_k u_j(\boldsymbol{r};\boldsymbol{r}_0) + \partial_j u_k(\boldsymbol{r};\boldsymbol{r}_0))\big] = 0, \quad \boldsymbol{r}\in\Omega_{ext}, \quad (56)\end{aligned}$$

where ∂_k represents the x_k-derivative, u_k is the k-th component of $\boldsymbol{u}$, and the Einstein summation convention is assumed.

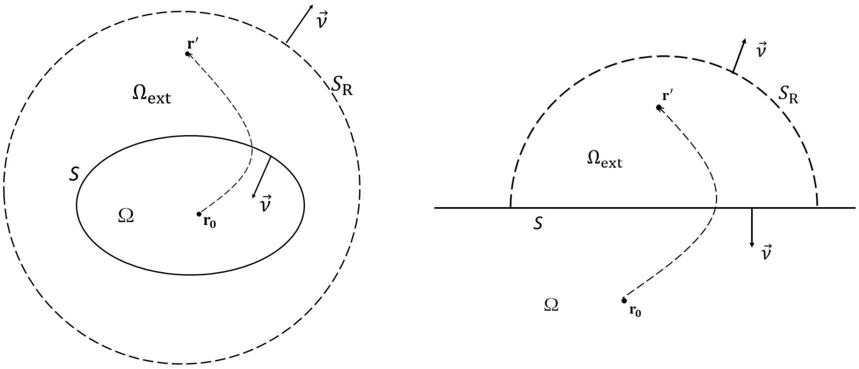

(a) (b)

Figure 4.1: Huygens-Kirchhoff formula for wave field extrapolation. (a) Spherical domains. (b) Planar domains.

Meanwhile, since the (k,l)-th element of the Green's tensor $\boldsymbol{G}(\boldsymbol{r};\boldsymbol{r}')$ excited by a source $\boldsymbol{r}' \in \Omega_{\mathrm{ext}}$ satisfies

$$\rho(\boldsymbol{r})\omega^2 G_{kl}(\boldsymbol{r};\boldsymbol{r}') + \partial_j\big[\lambda(\boldsymbol{r})\delta_{kj}\partial_m G_{ml}(\boldsymbol{r};\boldsymbol{r}') \\ + \mu(\boldsymbol{r})(\partial_k G_{jl}(\boldsymbol{r};\boldsymbol{r}') + \partial_j G_{kl}(\boldsymbol{r};\boldsymbol{r}'))\big] = -\delta_{kl}\delta(\boldsymbol{r}-\boldsymbol{r}') \tag{57}$$

for $1 \le k, l \le 3$, where δ_{kl} is the Kronecker delta, we have for the l-th element of u in Ω_{ext},

$$\begin{aligned} -u_l(\boldsymbol{r}';\boldsymbol{r}_0) &= \int_{\Omega_{ext}} -\delta_{kl}\delta(\boldsymbol{r}-\boldsymbol{r}')u_k(\boldsymbol{r};\boldsymbol{r}_0)d\boldsymbol{r} \\ &= \int_{\Omega_{ext}} \big\{\rho\omega^2 G_{kl} + \partial_j[\lambda\delta_{kj}\partial_m G_{ml} + \mu(\partial_k G_{jl} + \partial_j G_{kl})]\big\}u_k d\boldsymbol{r} \\ &= \int_{\Omega_{\mathrm{ext}}} \big\{\partial_j[\lambda\delta_{kj}\partial_m G_{ml} + \mu(\partial_k G_{jl} + \partial_j G_{kl})]u_k \\ &\qquad -\partial_j[\lambda\delta_{kj}\partial_m u_m + \mu(\partial_k u_j + \partial_j u_k)]G_{kl}\big\}d\boldsymbol{r}. \end{aligned} \tag{58}$$

Integrating by parts, we get

$$\begin{aligned} u_l(\boldsymbol{r}';\boldsymbol{r}_0) =& \int_{\Omega_{ext}} \big\{[\lambda\delta_{kj}\partial_m G_{ml} + \mu(\partial_k G_{jl} + \partial_j G_{kl})]\partial_j u_k \\ &\qquad - [\lambda\delta_{kj}\partial_m u_m + \mu(\partial_k u_j + \partial_j u_k)]\partial_j G_{kl}\big\}d\boldsymbol{r} \\ &- \int_{S+S_R} \big\{[\lambda\delta_{kj}\partial_m G_{ml} + \mu(\partial_k G_{jl} + \partial_j G_{kl})]u_k \\ &\qquad - [\lambda\delta_{kj}\partial_m u_m + \mu(\partial_k u_j + \partial_j u_k)]G_{kl}\big\}\nu_j dS(\boldsymbol{r}) \\ =& -\int_S \big\{\lambda[\partial_m G_{ml} u_j \nu_j - \partial_m u_m G_{jl}\nu_j] \\ &\qquad + \mu\nu_j[(\partial_k G_{jl} + \partial_j G_{kl})u_k - (\partial_k u_j + \partial_j u_k)G_{kl}]\big\}dS(\boldsymbol{r}) \end{aligned} \tag{59}$$

for $l = 1, 2, 3$, where $\boldsymbol{\nu} = (\nu_1, \nu_2, \nu_3)^T$ is the unit normal vector directing outward Ω_{ext}. The last equality holds since by letting $R \to \infty$, the integration on S_R vanishes by virtue of the imposed radiation condition.

Consequently, in vector notation, we have obtained the following equivalence of the Huygens-Kirchhoff formula,

$$\begin{aligned}\boldsymbol{u}(\boldsymbol{r}'; \boldsymbol{r}_0) = \int_S \Big\{ &\lambda[-(\nabla \cdot \boldsymbol{G})(\boldsymbol{u}(\boldsymbol{r}; \boldsymbol{r}_0) \cdot \boldsymbol{\nu}) + (\nabla \cdot \boldsymbol{u}(\boldsymbol{r}; \boldsymbol{r}_0))(\boldsymbol{G} \cdot \boldsymbol{\nu})] \\ &+ \mu[(\boldsymbol{\nu} \cdot \nabla)\boldsymbol{u}(\boldsymbol{r}; \boldsymbol{r}_0) \cdot \boldsymbol{G} - (\boldsymbol{\nu} \cdot \nabla)\boldsymbol{G} \cdot \boldsymbol{u}(\boldsymbol{r}; \boldsymbol{r}_0)] \\ &+ \mu[(\boldsymbol{G} \cdot \nabla)\boldsymbol{u}(\boldsymbol{r}; \boldsymbol{r}_0) \cdot \boldsymbol{\nu} - (\boldsymbol{u}(\boldsymbol{r}; \boldsymbol{r}_0) \cdot \nabla)\boldsymbol{G} \cdot \boldsymbol{\nu}] \Big\} dS(\boldsymbol{r}), \end{aligned} \tag{60}$$

on the boundary S of the domain Ω enclosing $\boldsymbol{r}_0$. The formula indicates that if the wave fields $\boldsymbol{u}(\boldsymbol{r}; \boldsymbol{r}_0)$ and the Green's tensor $\boldsymbol{G}(\boldsymbol{r}; \boldsymbol{r}')$ are known on the boundary S, then the wave fields $\boldsymbol{u}(\boldsymbol{r}'; \boldsymbol{r}_0)$ in the domain Ω_{ext} away from S can be constructed.

In particular, we are interested in the case when the boundary S is the plane at $z = z_0$, and the wave field is known in the domain $\Omega = \{z \le z_0\}$. In other words, we need to determine $\boldsymbol{u}$ in $\Omega_{\text{ext}} := \{\boldsymbol{r} = (x, y, z) | z > z_0\}$, and hence in this case, $\boldsymbol{\nu} = (0, 0, -1)^T$. Therefore, equation (59) reduces to

$$\begin{aligned}u_l(\boldsymbol{r}'; \boldsymbol{r}_0) = \int_{z=z_0} \Big\{ &\lambda(\boldsymbol{r})[\partial_m G_{ml}(\boldsymbol{r}; \boldsymbol{r}') u_3(\boldsymbol{r}; \boldsymbol{r}_0) - \partial_m u_m(\boldsymbol{r}; \boldsymbol{r}_0) G_{3l}(\boldsymbol{r}; \boldsymbol{r}')] \\ &+ \mu(\boldsymbol{r})(\partial_k G_{3l}(\boldsymbol{r}; \boldsymbol{r}') + \partial_3 G_{kl}(\boldsymbol{r}; \boldsymbol{r}')) u_k(\boldsymbol{r}; \boldsymbol{r}_0) \\ &- \mu(\boldsymbol{r})(\partial_k u_3(\boldsymbol{r}; \boldsymbol{r}_0) + \partial_3 u_k(\boldsymbol{r}; \boldsymbol{r}_0)) G_{kl}(\boldsymbol{r}; \boldsymbol{r}') \Big\} dxdy. \end{aligned} \tag{61}$$

Consequently, to obtain the (l, n)-th element of Green's tensor $\boldsymbol{G}(\boldsymbol{r}'; \boldsymbol{r}_0)$, $G_{ln}(\boldsymbol{r}'; \boldsymbol{r}_0)$, we can replace u_l with G_{ln} in equation (61). Then the corresponding Huygens-Kirchhoff formula for the Green's tensor $\boldsymbol{G}(\boldsymbol{r}'; \boldsymbol{r}_0)$ is

$$\begin{aligned}G_{ln}(\boldsymbol{r}'; \boldsymbol{r}_0) = \int_{z=z_0} \Big\{ &\lambda(\boldsymbol{r})[\partial_m G_{ml}(\boldsymbol{r}; \boldsymbol{r}') G_{3n}(\boldsymbol{r}; \boldsymbol{r}_0) - \partial_m G_{mn}(\boldsymbol{r}; \boldsymbol{r}_0) G_{3l}(\boldsymbol{r}; \boldsymbol{r}')] \\ &+ \mu(\boldsymbol{r})(\partial_k G_{3l}(\boldsymbol{r}; \boldsymbol{r}') + \partial_3 G_{kl}(\boldsymbol{r}; \boldsymbol{r}')) G_{kn}(\boldsymbol{r}; \boldsymbol{r}_0) \\ &- \mu(\boldsymbol{r})(\partial_k G_{3n}(\boldsymbol{r}; \boldsymbol{r}_0) + \partial_3 G_{kn}(\boldsymbol{r}; \boldsymbol{r}_0)) G_{kl}(\boldsymbol{r}; \boldsymbol{r}') \Big\} dxdy \end{aligned} \tag{62}$$

for $1 \le l, n \le 3$. Numerically, it is expensive to compute the Green's tensors $\boldsymbol{G}(\boldsymbol{r}; \boldsymbol{r}')$ excited by all $\boldsymbol{r}' \in \Omega_{ext}$ since the dimension of the manifold Ω_{ext} is higher than that of S. However, since the following reciprocal relations are satisfied

$$\tau(\boldsymbol{r}; \boldsymbol{r}') = \tau(\boldsymbol{r}'; \boldsymbol{r}), \quad \boldsymbol{G}(\boldsymbol{r}; \boldsymbol{r}') = \boldsymbol{G}^T(\boldsymbol{r}'; \boldsymbol{r}), \tag{63}$$

we can interchange the two arguments $\boldsymbol{r}$ and $\boldsymbol{r}'$ in $\boldsymbol{G}(\boldsymbol{r}'; \boldsymbol{r})$ in (62) to get

$$\begin{aligned}G_{ln}(\boldsymbol{r}'; \boldsymbol{r}_0) = \int_{z=z_0} \Big\{ &\lambda(\boldsymbol{r})[\partial_m G_{lm}(\boldsymbol{r}'; \boldsymbol{r}) G_{3n}(\boldsymbol{r}; \boldsymbol{r}_0) - \partial_m G_{mn}(\boldsymbol{r}; \boldsymbol{r}_0) G_{l3}(\boldsymbol{r}'; \boldsymbol{r})] \\ &+ \mu(\boldsymbol{r})(\partial_k G_{l3}(\boldsymbol{r}'; \boldsymbol{r}) + \partial_3 G_{lk}(\boldsymbol{r}'; \boldsymbol{r})) G_{kn}(\boldsymbol{r}; \boldsymbol{r}_0) \\ &- \mu(\boldsymbol{r})(\partial_k G_{3n}(\boldsymbol{r}; \boldsymbol{r}_0) + \partial_3 G_{kn}(\boldsymbol{r}; \boldsymbol{r}_0)) G_{lk}(\boldsymbol{r}'; \boldsymbol{r}) \Big\} dxdy, \end{aligned} \tag{64}$$

Without using the summation convention, we can rewrite formula (64) into the following,

$$\begin{aligned} G_{ln}(\boldsymbol{r}', \boldsymbol{r}_0) = \int_{z=z_0} \Big\{ & \lambda(\boldsymbol{r}) \sum_{m=1}^{3} [\partial_m G_{lm}(\boldsymbol{r}'; \boldsymbol{r}) G_{3n}(\boldsymbol{r}; \boldsymbol{r}_0) - \partial_m G_{mn}(\boldsymbol{r}; \boldsymbol{r}_0) G_{l3}(\boldsymbol{r}'; \boldsymbol{r})] \\ & + \mu(\boldsymbol{r})(\partial_1 G_{l3}(\boldsymbol{r}'; \boldsymbol{r}) + \partial_3 G_{l1}(\boldsymbol{r}'; \boldsymbol{r})) G_{1n}(\boldsymbol{r}; \boldsymbol{r}_0) \\ & + \mu(\boldsymbol{r})(\partial_2 G_{l3}(\boldsymbol{r}'; \boldsymbol{r}) + \partial_3 G_{l2}(\boldsymbol{r}'; \boldsymbol{r})) G_{2n}(\boldsymbol{r}; \boldsymbol{r}_0) \\ & + \mu(\boldsymbol{r})(\partial_3 G_{l3}(\boldsymbol{r}'; \boldsymbol{r}) + \partial_3 G_{l3}(\boldsymbol{r}'; \boldsymbol{r})) G_{3n}(\boldsymbol{r}; \boldsymbol{r}_0) \\ & - \mu(\boldsymbol{r})(\partial_1 G_{3j}(\boldsymbol{r}; \boldsymbol{r}_0) + \partial_3 G_{1n}(\boldsymbol{r}; \boldsymbol{r}_0)) G_{l1}(\boldsymbol{r}'; \boldsymbol{r}) \\ & - \mu(\boldsymbol{r})(\partial_2 G_{3j}(\boldsymbol{r}; \boldsymbol{r}_0) + \partial_3 G_{2n}(\boldsymbol{r}; \boldsymbol{r}_0)) G_{l2}(\boldsymbol{r}'; \boldsymbol{r}) \\ & - \mu(\boldsymbol{r})(\partial_2 G_{3j}(\boldsymbol{r}; \boldsymbol{r}_0) + \partial_3 G_{3n}(\boldsymbol{r}; \boldsymbol{r}_0)) G_{l3}(\boldsymbol{r}'; \boldsymbol{r}) \Big\} dxdy, \end{aligned} \tag{65}$$

As can be seen, the only unknowns in formula (65) are $\boldsymbol{G}(\boldsymbol{r}'; \boldsymbol{r})$ and its spatial derivatives. To use the truncated H-B ansatz to approximate $\boldsymbol{G}(\boldsymbol{r}'; \boldsymbol{r})$, we assume that caustics do not occur in the domain Ω_{ext}. By formulas (16) and (46), we may approximate

$$\begin{aligned} G_{kj}(\boldsymbol{r}'; \boldsymbol{r}) &= G^S_{kj}(\boldsymbol{r}'; \boldsymbol{r}) + G^P_{kj}(\boldsymbol{r}'; \boldsymbol{r}) \\ &\approx \frac{\tilde{A}^{S0}_{kj}(\boldsymbol{r}'; \boldsymbol{r})}{-\omega^2} f_{-3+\frac{1}{2}}(\omega, \tau^S(\boldsymbol{r}'; \boldsymbol{r})) + \frac{\tilde{A}^{S1}_{kj}(\boldsymbol{r}'; \boldsymbol{r})}{-\omega^2 {\tau^S}^2} f_{-2+\frac{1}{2}}(\omega, \tau^S(\boldsymbol{r}'; \boldsymbol{r})) \\ &+ \frac{\tilde{A}^{P0}_{kj}(\boldsymbol{r}'; \boldsymbol{r})}{-\omega^2} f_{-3+\frac{1}{2}}(\omega, \tau^P(\boldsymbol{r}'; \boldsymbol{r})) + \frac{\tilde{A}^{P1}_{kj}(\boldsymbol{r}'; \boldsymbol{r})}{-\omega^2 {\tau^P}^2} f_{-2+\frac{1}{2}}(\omega, \tau^P(\boldsymbol{r}'; \boldsymbol{r})). \end{aligned} \tag{66}$$

Then based on the formula (12) and the properties of Hankel functions, we can compute the spatial derivative of $\boldsymbol{G}^S(\boldsymbol{r}'; \boldsymbol{r})$ with respect to $\boldsymbol{r}$,

$$\begin{aligned} \partial_{x_i} G^S_{kj}(\boldsymbol{r}'; \boldsymbol{r}) \approx & \frac{2\tau^S \partial_{x_i} \tau^S \tilde{A}^{S0}_{kj}(\boldsymbol{r}'; \boldsymbol{r})}{\omega^2} f_{-4+\frac{1}{2}}(\omega, \tau^S(\boldsymbol{r}'; \boldsymbol{r})) \\ & + \left[\frac{\partial_{x_i} \tilde{A}^{S0}_{kj}(\boldsymbol{r}'; \boldsymbol{r})}{-\omega^2} + \frac{2\partial_{x_i} \tau^S \tilde{A}^{S1}_{kj}(\boldsymbol{r}'; \boldsymbol{r})}{\omega^2 \tau^S} \right] f_{-3+\frac{1}{2}}(\omega, \tau^S(\boldsymbol{r}'; \boldsymbol{r})) \\ & + \partial_{x_i} \left[\frac{\tilde{A}^{S1}_{kj}(\boldsymbol{r}'; \boldsymbol{r})}{-\omega^2 {\tau^S}^2} \right] f_{-2+\frac{1}{2}}(\omega, \tau^S(\boldsymbol{r}'; \boldsymbol{r})); \end{aligned} \tag{67}$$

the same can be done for $\boldsymbol{G}^P(\boldsymbol{r}'; \boldsymbol{r})$ to obtain $\partial_{x_i} \boldsymbol{G}^P(\boldsymbol{r}'; \boldsymbol{r})$. Because we have $f_{-3+l+\frac{1}{2}}(\omega, \tau) = O(\omega^{-l+2})$ as $\omega \to \infty$, retaining the only leading order terms, i.e. the $O(1)$ terms in (66) and $O(\omega)$ terms in (67), leads to the following approximations,

$$G^S_{kj}(\boldsymbol{r}'; \boldsymbol{r}) \approx \frac{\tilde{A}^{S0}_{kj}(\boldsymbol{r}'; \boldsymbol{r})}{8{\tau^S}^3(\boldsymbol{r}'; \boldsymbol{r})} e^{i\omega\tau^S(\boldsymbol{r}'; \boldsymbol{r})}, \tag{68}$$

$$\partial_{x_i} G^S_{kj}(\boldsymbol{r}'; \boldsymbol{r}) \approx \frac{i\omega \partial_{x_i} \tau^S(\boldsymbol{r}'; \boldsymbol{r}) \tilde{A}^{S0}_{kj}(\boldsymbol{r}'; \boldsymbol{r})}{8{\tau^S}^3(\boldsymbol{r}'; \boldsymbol{r})} e^{i\omega\tau^S(\boldsymbol{r}'; \boldsymbol{r})}; \tag{69}$$

similar approximations for the P-wave can be obtained accordingly.

Such approximations are adequately accurate for computing $\boldsymbol{G}(\boldsymbol{r}';\boldsymbol{r}_0)$ the formula (65) for the following reason. The integrand in the formula (65) is in general $O(\omega)$ and becomes $O(1)$ only when $\partial_{x_i}\boldsymbol{G}(\boldsymbol{r}';\boldsymbol{r}) = O(1)$ for all i and $\boldsymbol{G}(\boldsymbol{r}';\boldsymbol{r}) = O(1/\omega)$ (due to $\partial_{x_i}\boldsymbol{G}(\boldsymbol{r};\boldsymbol{r}_0) = O(\omega)$). Hence the approximations lose accuracy only when the approximations for both $\partial_{x_i}\boldsymbol{G}(\boldsymbol{r}';\boldsymbol{r})$ and $\boldsymbol{G}(\boldsymbol{r}';\boldsymbol{r})$ become 0 simultaneously, and the points with such a property constitute only a set of measure 0 and will not affect the value of $\boldsymbol{G}(\boldsymbol{r}';\boldsymbol{r}_0)$ in the formula (65).

As can be seen, the only unkowns in (68) and (69) are τ^S, $\tilde{\boldsymbol{A}}^{S0}$ and $\nabla_{\boldsymbol{r}}\tau^S(\boldsymbol{r}';\boldsymbol{r})$. Hence in order to obtain the Green's tensor $\boldsymbol{G}(\boldsymbol{r}';\boldsymbol{r}_0)$, we need to compute the asymptotic ingredients: τ^S, $\tilde{\boldsymbol{A}}^{S0}$ and $\nabla_{\boldsymbol{r}}\tau^S(\boldsymbol{r}';\boldsymbol{r})$ for the S-wave and τ^P, $\tilde{\boldsymbol{A}}^{P0}$ and $\nabla_{\boldsymbol{r}}\tau^P(\boldsymbol{r}';\boldsymbol{r})$ for the P-wave. In the previous section, we have shown how to compute the phase functions and H-B coefficients for both the S- and P-waves up to a suitable order of accuracy. The same methodology can be used here for all secondary sources.

Since $\nabla_{\boldsymbol{r}}\tau(\boldsymbol{r}';\boldsymbol{r})$ is opposite to the take-off direction $\boldsymbol{t}^{(0)}(\boldsymbol{r}',\boldsymbol{r})$ along the ray from $\boldsymbol{r}$ to $\boldsymbol{r}'$, where $\boldsymbol{t}^{(0)}(\boldsymbol{r}',\boldsymbol{r})$ is governed by the following equation

$$(\nabla_{\boldsymbol{r}'}\tau(\boldsymbol{r}';\boldsymbol{r}) \cdot \nabla_{\boldsymbol{r}'})\boldsymbol{t}^{(0)}(\boldsymbol{r}',\boldsymbol{r}) = 0, \tag{70}$$

with the initial condition $$\lim_{\boldsymbol{r}'\to\boldsymbol{r}}\left[\boldsymbol{t}^{(0)}(\boldsymbol{r}';\boldsymbol{r}) - \frac{\boldsymbol{r}'-\boldsymbol{r}}{|\boldsymbol{r}'-\boldsymbol{r}|}\right] = 0, \tag{71}$$

the high-order LxF-WENO schemes [22, 23] can be applied to first compute $\boldsymbol{t}^{(0)}$ for both the S- and P-waves, yielding $\nabla_{\boldsymbol{r}}\tau(\boldsymbol{r}';\boldsymbol{r})$ accordingly.

4.2. Huygens principle based sweeping method

Based on the Huygens-Kirchhoff formula, we now develop a layer-by-layer sweeping method to construct the globally valid Green's tensors.

The Green's tensor $\boldsymbol{G}$ as constructed by the ansatz (11) is valid only in a local neighborhood of $\boldsymbol{r}_0$ where no caustics occur since the computed ingredients in formula (11) are single-valued. Therefore, the integration formula (65) can only be used in a narrow layer where the Green's tensor $\boldsymbol{G}$ excited by every selected secondary source point $\boldsymbol{r} \in S$ is valid. However, since caustics will not develop close to a source in an isotropic medium, we can construct the entire elastic wave field excited from a primary point source in a global domain in a layer-by-layer manner.

Given a primary source $\boldsymbol{r}_0$, we can first construct the asymptotic Green's tensor $\boldsymbol{G}(\boldsymbol{r};\boldsymbol{r}_0)$ by substituting the already computed ingredients into the ansatz (11), which is valid in a local neighborhood Ω_1 containing the primary source $\boldsymbol{r}_0$; consequently, the Green's function $\boldsymbol{G}(\boldsymbol{r};\boldsymbol{r}_0)$ and its gradient $\nabla\boldsymbol{G}(\boldsymbol{r};\boldsymbol{r}_0)$ is known on the boundary of Ω_1, denoted by S_1. Letting Ω_1 be the first layer, we can set up secondary point sources on the boundary S_1, and identify a narrow layer, denoted by Ω_2, where the Green's functions $\boldsymbol{G}(\boldsymbol{r}';\boldsymbol{r})$ ($\boldsymbol{r} \in S_1$, $\boldsymbol{r}' \in \Omega_2$) are locally valid. The method of identifying the narrow layer will be addressed later. Then we can apply the integration formula (65) to construct the Green's function $\boldsymbol{G}(\boldsymbol{r}';\boldsymbol{r}_0)$ in the layer Ω_2, so that $\boldsymbol{G}(\boldsymbol{r}';\boldsymbol{r}_0)$ and $\nabla\boldsymbol{G}(\boldsymbol{r}';\boldsymbol{r}_0)$ are available on $S_2 = \partial\Omega_2$. The process can be repeated so that the Green's functions can be constructed everywhere by sweeping through the whole domain in a layer-by-layer fashion.

As addressed in [23, 26, 32], the method of partitioning the whole computational domain into layers is based on the first-arrival traveltime solutions for both the S- and P-wave eikonal equations with point-source conditions. Suppose that the traveltime solutions, $\tau^S(\boldsymbol{r};\boldsymbol{r}_0)$ and $\tau^P(\boldsymbol{r};\boldsymbol{r}_0)$, are computed in the whole domain, we can determine the first layer Ω_1 as the neighborhood of $\boldsymbol{r}_0$ where both $\tau^S(\boldsymbol{r};\boldsymbol{r}_0)$ and $\tau^P(\boldsymbol{r};\boldsymbol{r}_0)$ are smooth. Then we can set up a few secondary-source points on the boundary S_1 of the first layer, solve both the S- and P-wave point-source eikonal equations at those secondary sources to obtain first-arrival traveltimes, and determine a local neighborhood where all those traveltimes from both the S- and P-wave eikonal equations are smooth. This neighborhood will serve as the second narrow layer Ω_2. The process can be repeated so that the whole domain will be covered by all such layers.

Since the Green's functions are singular at the source point, we will use the Huygens-Kirchhoff formula (65) to compute the Green's functions $\boldsymbol{G}$ at observation points away from the secondary source surface. To well separate the receiver domain and the secondary source surface, we can move the secondary source surface slightly closer to the primary source, and the missing portion of the Green's functions is already computed by either using the primary source or using the previous layer.

Since, in practice, we are interested in designing methods with efficiency independent of frequency, we will set a fixed distance $d_f \geq 0$ to separate the secondary source surface and the receiver domain; the reason is that when the frequency parameter ω is big enough, the asymptotic Green's functions become accurate roughly away from the source by this distance.

4.3. Planar-layer based Huygens sweeping

To better illustrate the sweeping process, we consider the wave fields directed along the positive z-direction. As shown in Figure 4.2, the computational domain is partitioned into some non-overlapping layers Ω_j, where all secondary-source surfaces S_j are planar and perpendicular to the z-direction, and this partition satisfies the properties discussed above. The planar-based sweeping method can be summarized as the following.

Algorithm 1

Stage 1. Precompute asymptotic ingredients.

- The computational domain is partitioned into layers Ω_j and the secondary-source planes S_j are identified using the above approach.
- For each secondary source plane S_j, the tables of traveltime, amplitudes and take-off directions are computed at each secondary source on a coarse mesh in the layer Ω_{j+1}. In practice, those tables can be computed for a coarse set of secondary sources since the tables on a dense set of secondary sources can be obtained by interpolating those coarse tables.
- The tables for the coarse set of secondary sources are stored (on a hard drive) and can be used to construct the wave fields for all high frequencies and for arbitrary point sources.

Stage 2. Given a free-space frequency ω, construct the wave field layer by layer.

- For each secondary source plane S_j, the tables of the traveltimes, amplitudes and take-off directions for both the S- and P-wave are loaded from the hard drive to construct the Green's function $\boldsymbol{G}(\boldsymbol{r};\boldsymbol{r}_0)$ in the corresponding layer Ω_{j+1}.

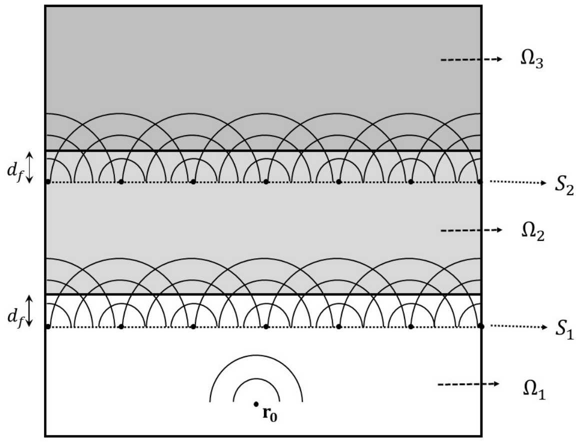

Figure 4.2: The computational domain is partitioned into three layers: Ω_1, Ω_2, and Ω_3. The first layer Ω_1 contains the primary source $\boldsymbol{r}_0$; the source plane S_1 is placed in Ω_1 and is d_f wide away from Ω_2; the source plane S_2 is d_f wide away from Ω_3 and locates in Ω_2.

- For each table, the data are first interpolated onto a finer mesh to resolve the highly oscillatory nature of $\boldsymbol{G}$ and then compute $\boldsymbol{G}(\boldsymbol{r};\boldsymbol{r}_0)$ by the Huygens-Kirchhoff formula with a quadrature rule.
- If the sampling of secondary sources on the source plane S_j is not dense enough, we can interpolate the tables from the given source locations onto the region bounded by these source locations. This is feasible because asymptotic ingredients are continuous functions of source locations. For instance, given the four source points s_A, s_B, s_C and s_D which are vertices of a rectangular region $ABCD$ of the mesh on S_j, and at which the tables are computed and are already interpolated onto finer mesh in the corresponding layer, we can interpolate the four tables to find the table at any source point inside the rectangular region $ABCD$.

To implement the above algorithm, we need to overcome some obstacles. The first obstacle is how to store the data tables generated in Stage 1 since there are many sources in the source plane S_j and also we are dealing with nine-component Green's functions for 3-D elastic wave equations. The second obstacle is how to efficiently carry out the matrix-vector products induced by the discretization of the Huygens-Kirchhoff integral (65). We will address these two issues in the following subsections.

4.4. Data tables and compression

To reduce data storage, we will follow the approach in [33] to compress each data table into a linear combination of tensor product based multivariate Chebyshev polynomials so that information in each table is encoded into a small number of

Chebyshev coefficients. In our implementation, we need to compress the data tables for both the S- and P-wave related ingredients separately.

To efficiently reconstruct the information from those compressed tables, we will follow the method in [33] which is equivalent to Orszag's partial summation method [6].

4.5. Discretization of Huygens-Kirchhoff integral

In numerical implementation, it is difficult to evaluate the (k, j)-entry of the Green's function $\boldsymbol{G}(\boldsymbol{r};\boldsymbol{r}_0)$ by the equation (65) for $k, j = 1, 2, 3$, when the secondary-source plane is unbounded. Hence, first we need to truncate the unbounded integration domain S to a finite, bounded domain $\tilde{S}$ according to the specified computational domain for elastic wave equations. Since the expansion (11) automatically exhibits outgoing wave behavior and satisfies the Sommerfeld radiation condition at infinity, such a truncation may slightly affect the accuracy of the wave field near the boundary of $\tilde{S}$ only.

After truncation, the bounded domain $\tilde{S}$ can be discretized so that the quadrature rule can be applied to approximate the integral in (65). Since we are interested in computing highly oscillatory waves, we have to specify sufficient mesh points to sample the overall solution. In principle, the optimal number of sampling points is arguably four to six mesh points per wavelength in each direction. However, in the high-frequency regime, the direct methods such as finite-difference or finite-element methods require many more points per wavelength so as to yield accurate numerical solutions due to pollution or dispersion errors [4, 5]. On the other hand, the H-B ansatz based method requires only four to six mesh points per wavelength to resolve the overall solution in the high-frequency regime and this has been verified in [32, 34] and in the following examples.

Since given the index of refraction γ and the frequency parameter ω, the smallest wavelength in the computational domain can be estimated to be $\lambda_{\max} = 2\pi/\omega\gamma_{\max}$, where $\gamma_{\max}$ is the largest value of both γ^S and γ^P in the computational domain, and we specify 4 to 6 points per wavelength in each direction accordingly. We remark that because all the ingredients in the H-B ansatz are independent of frequency, one can compute these asymptotic ingredients on much coarser meshes with the number of points independent of frequency. Only when we construct the overall wave fields do we need to interpolate those ingredients onto the fine meshes so as to capture each wave accurately.

Based on the above considerations, we are ready to discretize the integral (65). Assume that the primary point source $\boldsymbol{r}_0$ is given, and the truncated rectangular region $\tilde{S}$ is discretized into a set of $M_s = M_x \times M_y$ uniform grid points with the same mesh size h in both x- and y-directions so that the above sampling requirement of four to six points per wavelength is satisfied. We apply the trapezoidal rule to approximate the integral over $\tilde{S}$ and obtain

$$\begin{aligned} G_{kj}(\boldsymbol{r}',\boldsymbol{r}_0) \approx h^2 \sum_{m=1}^{Mx''}\sum_{n=1}^{My''}\Big[&\lambda(\boldsymbol{s}_{mn})\sum_{m=1}^{3}(\partial_m G_{km}(\boldsymbol{r}';\boldsymbol{s}_{mn})G_{3j}(\boldsymbol{s}_{mn};\boldsymbol{r}_0) \\ &- \lambda(\boldsymbol{s}_{mn})\sum_{m=1}^{3}\partial_m G_{mj}(\boldsymbol{s}_{mn};\boldsymbol{r}_0)G_{k3}(\boldsymbol{r}';\boldsymbol{s}_{mn})) \end{aligned}$$

$$
\begin{aligned}
&+ \mu(\boldsymbol{s}_{mn})(\partial_1 G_{k3}(\boldsymbol{r}'; \boldsymbol{s}_{mn}) + \partial_3 G_{k1}(\boldsymbol{r}'; \boldsymbol{s}_{mn}))G_{1j}(\boldsymbol{s}_{mn}; \boldsymbol{r}_0) \\
&+ \mu(\boldsymbol{s}_{mn})(\partial_2 G_{k3}(\boldsymbol{r}'; \boldsymbol{s}_{mn}) + \partial_3 G_{k2}(\boldsymbol{r}'; \boldsymbol{s}_{mn}))G_{2j}(\boldsymbol{s}_{mn}; \boldsymbol{r}_0) \\
&+ \mu(\boldsymbol{s}_{mn})(\partial_3 G_{k3}(\boldsymbol{r}'; \boldsymbol{s}_{mn}) + \partial_3 G_{k3}(\boldsymbol{r}'; \boldsymbol{s}_{mn}))G_{3j}(\boldsymbol{s}_{mn}; \boldsymbol{r}_0) \\
&- \mu(\boldsymbol{s}_{mn})(\partial_1 G_{3j}(\boldsymbol{s}_{mn}; \boldsymbol{r}_0) + \partial_3 G_{1j}(\boldsymbol{s}_{mn}; \boldsymbol{r}_0))G_{k1}(\boldsymbol{r}'; \boldsymbol{s}_{mn}) \\
&- \mu(\boldsymbol{s}_{mn})(\partial_2 G_{3j}(\boldsymbol{s}_{mn}; \boldsymbol{r}_0) + \partial_3 G_{2j}(\boldsymbol{s}_{mn}; \boldsymbol{r}_0))G_{k2}(\boldsymbol{r}'; \boldsymbol{s}_{mn}) \\
&- \mu(\boldsymbol{s}_{mn})(\partial_3 G_{3j}(\boldsymbol{s}_{mn}; \boldsymbol{r}_0) + \partial_3 G_{3j}(\boldsymbol{s}_{mn}; \boldsymbol{r}_0))G_{k3}(\boldsymbol{r}'; \boldsymbol{s}_{mn})\Big]
\end{aligned}
\tag{72}
$$

for $k, j = 1, 2, 3$, where $\sum''$ denotes that the first and last term have a factor $\frac{1}{2}$.

We remark that here partial derivatives of $\boldsymbol{G}(\boldsymbol{s}_{mn}; \boldsymbol{r}_0)$ are estimated by numerical differentiation since the Green's functions $\boldsymbol{G}(\boldsymbol{r}; \boldsymbol{r}_0)$ are already computed and thus available. M_x and M_y are the number of grid points in the x- and y-directions, respectively; $\{\boldsymbol{s}_{mn}\}$ are the M_s mesh points on the source plane $\tilde{S}$, and are re-enumerated as $\{\boldsymbol{s}_m\}_{m=1}^{M_s}$.

According to the partition strategy, we are interested in evaluating (72) for all observation points in a narrow layer which is about d_f distance away from the source plane and we enumerate those mesh points as $\{\boldsymbol{r}_n\}_{n=1}^{N_r}$. Then we obtain

$$
\begin{aligned}
\boldsymbol{g}_{kj} = {} & \boldsymbol{U}_{k1}\boldsymbol{f}_{1j} + \boldsymbol{U}_{k2}\boldsymbol{f}_{2j} + \boldsymbol{U}_{k3}\boldsymbol{f}_{3j} + \boldsymbol{U}_{k4}\boldsymbol{f}_{4j} + \\
& + \boldsymbol{U}_{k5}\boldsymbol{f}_{5j} + \boldsymbol{U}_{k6}\boldsymbol{f}_{6j} + \boldsymbol{U}_{k7}\boldsymbol{f}_{7j} + \boldsymbol{U}_{k8}\boldsymbol{f}_{8j}
\end{aligned}
\tag{73}
$$

for $k, j = 1, 2, 3$, where

$$
\begin{aligned}
\boldsymbol{g}_{kj} &= \Big[G_{kj}(\boldsymbol{r}_1; \boldsymbol{r}_0), G_{kj}(\boldsymbol{r}_2; \boldsymbol{r}_0), \cdots, G_{kj}(\boldsymbol{r}_{N_r}; \boldsymbol{r}_0)\Big]^T, \\
\boldsymbol{U}_{k1} &= [\sum_{l=1}^{3} \partial_l G_{kl}(\boldsymbol{r}_n; \boldsymbol{s}_m)]_{1 \le n \le N_r, 1 \le m \le M_s}, \\
\boldsymbol{U}_{k2} &= [G_{k3}(\boldsymbol{r}_n; \boldsymbol{s}_m)]_{1 \le n \le N_r, 1 \le m \le M_s}, \\
\boldsymbol{U}_{k3} &= [\partial_1 G_{k3}(\boldsymbol{r}_n; \boldsymbol{s}_n) + \partial_3 G_{k1}(\boldsymbol{r}_n; \boldsymbol{s}_m)]_{1 \le n \le N_r, 1 \le m \le M_s}, \\
\boldsymbol{U}_{k4} &= [\partial_2 G_{k3}(\boldsymbol{r}_n; \boldsymbol{s}_m) + \partial_3 G_{k2}(\boldsymbol{r}_n; \boldsymbol{s}_m)]_{1 \le n \le N_r, 1 \le m \le M_s}, \\
\boldsymbol{U}_{k5} &= [\partial_3 G_{k3}(\boldsymbol{r}_n; \boldsymbol{s}_m) + \partial_3 G_{k3}(\boldsymbol{r}_n; \boldsymbol{s}_m)]_{1 \le n \le N_r, 1 \le m \le M_s}, \\
\boldsymbol{U}_{k6} &= [G_{k1}(\boldsymbol{r}_n; \boldsymbol{s}_m)]_{1 \le n \le N_r, 1 \le m \le M_s}, \\
\boldsymbol{U}_{k7} &= [G_{k2}(\boldsymbol{r}_n; \boldsymbol{s}_m)]_{1 \le n \le N_r, 1 \le m \le M_s}, \\
\boldsymbol{U}_{k8} &= [G_{k3}(\boldsymbol{r}_n; \boldsymbol{s}_m)]_{1 \le n \le N_r, 1 \le m \le M_s}, \\
\boldsymbol{f}_{1j} &= \Big[\lambda(\boldsymbol{s}_1)G_{3j}(\boldsymbol{s}_1; \boldsymbol{r}_0), \cdots, \lambda(\boldsymbol{s}_{M_s})G_{3j}(\boldsymbol{s}_{M_s}; \boldsymbol{r}_0)\Big]^T, \\
\boldsymbol{f}_{2j} &= -[\lambda(\boldsymbol{s}_1)\sum_{l=1}^{3} \partial_l G_{lj}(\boldsymbol{s}_1; \boldsymbol{r}_0), \cdots, \lambda(\boldsymbol{s}_{M_s})\sum_{l=1}^{3} \partial_l G_{lj}(\boldsymbol{s}_{M_s}; \boldsymbol{r}_0)]^T, \\
\boldsymbol{f}_{3j} &= [\mu(\boldsymbol{s}_1)G_{1j}(\boldsymbol{s}_1; \boldsymbol{r}_0), \cdots \mu(\boldsymbol{s}_{M_s})G_{1j}(\boldsymbol{s}_{M_s}; \boldsymbol{r}_0)]^T, \\
\boldsymbol{f}_{4j} &= [\mu(\boldsymbol{s}_1)G_{2j}(\boldsymbol{s}_1; \boldsymbol{r}_0), \cdots \mu(\boldsymbol{s}_{M_s})G_{2j}(\boldsymbol{s}_{M_s}; \boldsymbol{r}_0)]^T, \\
\boldsymbol{f}_{5j} &= [\mu(\boldsymbol{s}_1)G_{3j}(\boldsymbol{s}_1; \boldsymbol{r}_0), \cdots \mu(\boldsymbol{s}_{M_s})G_{3j}(\boldsymbol{s}_{M_s}; \boldsymbol{r}_0)]^T,
\end{aligned}
$$

$$
\begin{aligned}
\boldsymbol{f}_{6j} &= [-\mu(\boldsymbol{s}_1)(\partial_1 G_{3j}(\boldsymbol{s}_1;\boldsymbol{r}_0) + \partial_3 G_{1j}(\boldsymbol{s}_1;\boldsymbol{r}_0)), \cdots, -\mu(\boldsymbol{s}_{M_s})(\partial_1 G_{3j}(\boldsymbol{s}_{M_s};\boldsymbol{r}_0) \\
&\quad + \partial_3 G_{1j}(\boldsymbol{s}_{M_s};\boldsymbol{r}_0))]^T, \\
\boldsymbol{f}_{7j} &= [-\mu(\boldsymbol{s}_1)(\partial_2 G_{3j}(\boldsymbol{s}_1;\boldsymbol{r}_0) + \partial_3 G_{2j}(\boldsymbol{s}_1;\boldsymbol{r}_0)), \cdots, -\mu(\boldsymbol{s}_{M_s})(\partial_1 G_{3j}(\boldsymbol{s}_{M_s};\boldsymbol{r}_0) \\
&\quad + \partial_3 G_{1j}(\boldsymbol{s}_{M_s};\boldsymbol{r}_0))]^T, \\
\boldsymbol{f}_{8j} &= [-\mu(\boldsymbol{s}_1)(\partial_3 G_{3j}(\boldsymbol{s}_1;\boldsymbol{r}_0) + \partial_3 G_{3j}(\boldsymbol{s}_1;\boldsymbol{r}_0)), \cdots, -\mu(\boldsymbol{s}_{M_s})(\partial_1 G_{3j}(\boldsymbol{s}_{M_s};\boldsymbol{r}_0) \\
&\quad + \partial_3 G_{1j}(\boldsymbol{s}_{M_s};\boldsymbol{r}_0))]^T.
\end{aligned}
$$

In numerical implementation, we will uniformly and coarsely sample the secondary sources so that the asymptotic ingredients for those coarsely sampled sources are efficiently precomputed. In the high-frequency regime, we need to sample enough points on the source plane with finer meshes so as to obtain the desired accuracy. The asymptotic ingredients on those finer meshes can be obtained by interpolation.

To evaluate equation (73), we need to carry out total 72 matrix-vector multiplications for 9 components of $\boldsymbol{G}$. In practice, M_s and N_r could be extremely large for high frequencies so that the direct evaluation of (73) with complexity $O(M_s \times N_r)$ is expensive and impractical. To accelerate the evaluation process, we will use a multilevel matrix decomposition based butterfly algorithm as developed in [7, 23, 26, 28, 29, 32, 43]; see [8] for necessity of using such a method.

4.6. A butterfly algorithm

We can reformulate equation (73) as the following,

$$
g_{kj}(\boldsymbol{r}) = \sum_{q=1}^{8} \sum_{\boldsymbol{s}\in\boldsymbol{X}_s} U_{kq}(\boldsymbol{r};\boldsymbol{s}) f_{qj}(\boldsymbol{s}), \quad \boldsymbol{r} \in \boldsymbol{X}_r \subset \Omega_r, \tag{74}
$$

where $1 \le k, j \le 3$. Here the set of sources $\boldsymbol{X}_s$ is in the domain Ω_s, and the set of receivers $\boldsymbol{X}_r$ is in the domain Ω_r. Ω_s and Ω_r are d_f apart from each other. f_{qj} is the representative function of $\boldsymbol{f}_{qj}$ in the sense that $f_{qj}(\boldsymbol{s}_m)$ is the mth element of $\boldsymbol{f}_{qj}$ for $1 \le m \le M_s$. $U_{kq}(\boldsymbol{r};\boldsymbol{s})$ is the representative function of $\boldsymbol{U}_{kq}$.

Since, in (73), for each secondary source $\boldsymbol{s}_m$ and receiver $\boldsymbol{r}_n$, where $1 \le m \le M_s$, $1 \le n \le N_r$, the Green's tensor $\boldsymbol{G}(\boldsymbol{r}_n;\boldsymbol{s}_m)$ has the decomposition

$$
\boldsymbol{G}(\boldsymbol{r}_n;\boldsymbol{s}_m) = \boldsymbol{G}^S(\boldsymbol{r}_n;\boldsymbol{s}_m) + \boldsymbol{G}^P(\boldsymbol{r}_n;\boldsymbol{s}_m).
$$

Hence the representative function $U_{kq}(\boldsymbol{r};\boldsymbol{s})$ can be decomposed as follows:

$$
U_{kq}(\boldsymbol{r};\boldsymbol{s}) = U_{kq}^S(\boldsymbol{r};\boldsymbol{s}) + U_{kq}^P(\boldsymbol{r};\boldsymbol{s}) = A_{kq}^S(\boldsymbol{r};\boldsymbol{s}) e^{i\omega\tau^S(\boldsymbol{r};\boldsymbol{s})} + A_{kq}^P(\boldsymbol{r};\boldsymbol{s}) e^{i\omega\tau^P(\boldsymbol{r};\boldsymbol{s})}, \tag{75}
$$

where the amplitude $A_{kq}^S(\boldsymbol{r};\boldsymbol{s})$ and the traveltime $\tau^S(\boldsymbol{r};\boldsymbol{s})$ for the S-wave are available from equations (68) and (69). $A_{kq}^P(\boldsymbol{r};\boldsymbol{s})$ and $\tau^P(\boldsymbol{r};\boldsymbol{s})$ for the P-wave can be obtained in the same way. Then it is clear that we have

$$
g_{kj}(\boldsymbol{r}) = g_{kj}^S(\boldsymbol{r}) + g_{kj}^P(\boldsymbol{r}) \tag{76}
$$

with

$$
g_{kj}^S(\boldsymbol{r}) = \sum_{q=1}^{8} \sum_{\boldsymbol{s}\in\boldsymbol{X}_s} U_{kq}^S(\boldsymbol{r};\boldsymbol{s}) f_{qj}(\boldsymbol{s}) \quad \text{and} \quad g_{kj}^P(\boldsymbol{r}) = \sum_{q=1}^{8} \sum_{\boldsymbol{s}\in\boldsymbol{X}_s} U_{kq}^P(\boldsymbol{r};\boldsymbol{s}) f_{qj}(\boldsymbol{s}). \tag{77}
$$

Based on the decomposition in (75), we can follow [7, 23, 27, 32] to adopt the low-rank separated-representation based butterfly algorithm to speed up the matrix-vector multiplication for both g^S_{kj} and g^P_{kj}. In implementation, we can first use the butterfly algorithm to compute g^S_{kj} and then g^P_{kj}. Next, we can add g^S_{kj} and g^P_{kj} together to obtain g_{kj}. For the sake of convenience, in the following presentation we will suppress the superscripts S and P since the methodology works in the same way for computing both g^S_{kj} and g^P_{kj}.

To begin with, we first introduce the multi-dimensional Lagrange basis with respect to the Chebyshev nodes. For a given integer $p > 0$, the Chebyshev nodes of order p on the standard interval $[-1, 1]$ are

$$X = \left\{ x_j = \cos\left(\frac{(j-1)\pi}{p-1}\right)\right\}_{j=1}^{p}. \tag{78}$$

The j-th Lagrange basis function at $x \in [-1, 1]$ with nodes X is denoted as $L_X(x; x_j)$, which takes 1 at x_j and 0 elsewhere in X for $j = 1, \cdots, p$. Then the Chebyshev nodes of order p on the d-dimensional box $[-1, 1]^d$ are d tensor products of X,

$$X^d = \{x^1_{j_1}\}^p_{j_1=1} \times \cdots \times \{x^d_{j_d}\}^p_{j_d=1}. \tag{79}$$

Thus, letting $\boldsymbol{j} = (j_1, \cdots, j_d)$, the $\boldsymbol{j}$-th Lagrange basis function with nodes X^d at $\boldsymbol{x} = (x^1, \cdots, x^d)^T \in [-1, 1]^d$ is given as a tensor product,

$$L^d_{X^d}(\boldsymbol{x}; \boldsymbol{x_j}) = L_X(x^1; x^1_{j_1}) \cdots L_X(x^d; x^d_{j_d}), \tag{80}$$

where $\boldsymbol{x_j} = (x^1_{j_1}, \cdots, x^1_{j_d})^T$.

For a generic one-dimensional interval $[a, b]$, the Chebyshev nodes of order p satisfy

$$Y = \left\{ y_j = \frac{b-a}{a} x_j + \frac{b+a}{2}\right\}_{j=1}^{p}, \tag{81}$$

so that the j-th Lagrange basis function at $y \in [a, b]$ with nodes Y is denoted as $L_Y(y; y_j)$ for $j = 1, \cdots, p$. Similarly, the Chebyshev nodes of order p are d-tensor products of the form

$$\boldsymbol{Y} = Y_1 \times \cdots \times Y_d \tag{82}$$

with

$$Y_i = \left\{ y^i_{j_i} = \frac{b-a}{a} x^i_{j_i} + \frac{b+a}{2}\right\}_{j_i=1}^{p}. \tag{83}$$

Thus, the $\boldsymbol{j}$-th Lagrange basis function with nodes at $\boldsymbol{y} = (y^1, \cdots, y^d)^T \in [-1, 1]^d$ is given as

$$L^d_{\boldsymbol{Y}}(\boldsymbol{y}; \boldsymbol{y_j}) = L_{Y_1}(y^1; y^1_{j_1}) \cdots \times L_{Y_d}(y^d; y^d_{j_d}). \tag{84}$$

In the following, we will denote by $\boldsymbol{C}^B$ the set of p^d d-dimensional Chebyshev nodes in the d-dimensional box B. Following closely the butterfly algorithm in [27, 32], we present our algorithm as follows:

Algorithm 2. (The butterfly algorithm)

1. **Construct** the cluster trees for both receivers and sources. Assume that the domain of receivers is a cube $\Omega_r = [\mathcal{L}^r_{min}, \mathcal{L}^r_{max}]^3$, and the domain of sources is a square $\Omega_s = [\mathcal{L}^s_{min}, \mathcal{L}^s_{max}]^2$. The domains are discretized such that the number of sampling points per wavelength is fixed, such as 4 to 6 points per wavelength. The cluster trees for receivers and sources are an octree and a quadtree, respectively.

   At the root level (denote as level 0), the boxes for both the source and receiver cluster trees are assigned to the corresponding domain directly. Then the tree construction goes by dydically subdividing the boxes: for an octree (quadtree), each box is divided into 8 (4) boxes. The construction reaches or stops at the leaf level (denoted as level L), where the size of each box is about 2 minimum wavelengths so that approximately $O(p)$ sampling points are used along each dimension with p the order of Chebyshev nodes. Hence except for the leaf level, each box B of an octree (quadtree) has 8(4) children boxes, denoted as B^c, and except for the root level, each box B has a parent box, denoted as B^p. We denote the resulting two trees as T_s (the source tree) and T_r (the receiver tree), respectively. From now on, we will use the superscript $(\cdot)^B$ to denote the dependence on the box B.

   The butterfly algorithm traverses through the two cluster trees in the following way: for $l = L \cdots, 0$, visit level l in T_s and level $L - l$ in T_r by considering each pair $\{B_r, B_s\}$ with $B_r \in T^r$ and $B_s \in T^s$, $l(B_s) = l$ and $l(B^r) = L - l$, where $l(B)$ indicates the level of B in a tree.

   Moreover at the root level of the receiver tree and at the leaf level of the source tree, each pair $\{B_r, B_s\}$ satisfies

$$\begin{aligned}\mathrm{w}(B_r)\mathrm{w}(B_s) &= (\mathcal{L}^r_{\max} - \mathcal{L}^r_{\min})O(2\lambda_{\min}) \\ &= O\left(\frac{4\pi(\mathcal{L}^r_{\max} - \mathcal{L}^r_{\min})}{\omega\gamma_{\max}}\right) = O\left(\frac{1}{\omega}\right), \end{aligned} \tag{85}$$

   where $\mathrm{w}(B)$ is the size of box B and $\gamma_{\max} = \max(\gamma^S_{\max}, \gamma^P_{\max})$. $\gamma^S_{\max}$ and $\gamma^P_{\max}$ are the maximum slowness for the S- and P-waves, respectively. As moving downward the receiver tree by one level and simultaneously moving upward the source tree by one level, $\mathrm{w}(B_r)$ is divided by 2 while $\mathrm{w}(B_s)$ is multiplied by 2 so that the low-rank separated-representation condition $\mathrm{w}(B_r)\mathrm{w}(B_s) = O(\frac{1}{\omega})$ is automatically satisfied.

2. The **Upward Pass** starts at the leaf level (level L) of the source tree T_s and ends at the level (denoted as L_s), where the size of the boxes satisfies $\mathrm{w}(B_s) \geq O(\frac{1}{\sqrt{\omega}})$. Correspondingly, the level of the receiver tree T_r varies from the root level (level 0) to the level $L_r \equiv L - L_s$.

   (1) **Initialization:** For each pair $\{B_r, B_s\}$ with B_r traversing all boxes at the root level of the receiver tree and B_s traversing all boxes at the leaf level of the source tree, we interpolate 24 equivalent densities $\{\bar{f}^{B_r,B_s}_{qj}\}$ for $1 \leq q \leq 8$ and $1 \leq j \leq 3$ at the equivalent sources $\boldsymbol{C}^{B_s} = \{\boldsymbol{s}^{B_s}_n\}^{p^2}_{n=1}$ in B_s from the given 24 densities $\{f_{qj}\}$ at all sources in $B_s \cap \boldsymbol{X}_s$:

$$\bar{f}_{qj}^{B_r,B_s}(\boldsymbol{s}_n^{B_s}) = \sum_{\boldsymbol{s}\in B_s\cap \boldsymbol{X}_s} e^{-i\omega\tau(\boldsymbol{r}_c^{B_r};\boldsymbol{s}_n^{B_s})} L^2_{\boldsymbol{C}^{B_s}}(\boldsymbol{s};\boldsymbol{s}_n^{B_s}) e^{i\omega\tau(\boldsymbol{r}_c^{B_r};\boldsymbol{s})} f_{qj}(\boldsymbol{s}), \tag{86}$$

where $\boldsymbol{r}_c^{B_r}$ is the center of the receiver box B_r.

(2) **Recursion:** For l from $L-1$ to L_s, for each pair $\{B_r, B_s\}$ with B_r traversing all boxes at the level $L-l$ of the receiver tree and B_s traversing all boxes at the level l of the source tree, we interpolate 24 equivalent densities $\{\bar{f}_{qj}^{B_r,B_s}\}$ at the equivalent sources $\boldsymbol{C}^{B_s} = \{\boldsymbol{s}_n^{B_s}\}_{n=1}^{p^2}$ in B_s from the equivalent densities $\{\bar{f}_{qj}^{B_r^p,B_s^c}\}$ at equivalent sources $\boldsymbol{C}^{B_s^c} = \{\boldsymbol{s}_m^{B_s^c}\}_{m=1}^{p^2}$ of all the children clusters of B_s and the parent cluster of B_r:

$$\begin{aligned} &\bar{f}_{qj}^{B_r,B_s}(\boldsymbol{s}_n^{B_s}) = \\ &= \sum_{B_s^c}\sum_{m=1}^{P^2} e^{-i\omega\tau(\boldsymbol{r}_c^{B_r};\boldsymbol{s}_n^{B_s})} L^2_{\boldsymbol{C}^{B_s}}(\boldsymbol{s}_m^{B_s^c};\boldsymbol{s}_n^{B_s}) e^{i\omega\tau(\boldsymbol{r}_c^{B_r};\boldsymbol{s}_m^{B_s^c})} \bar{f}_{qj}^{B_r^p,B_s^c}(\boldsymbol{s}_m^{B_s^c}), \end{aligned} \tag{87}$$

for $1 \le q \le 8$ and $1 \le j \le 3$.

3. **Switch** at the level where the upward pass has ended (Level L_s of the source tree and level L_r of the receiver tree). For each pair $\{B_r, B_s\}$ with B_r traversing all boxes at the level L_r of the receiver tree and B_s traversing all boxes at the level L_s of the source tree, compute 9 equivalent fields $\{\bar{g}_{kj}^{B_r,B_s}\}$ at equivalent points $\boldsymbol{C}^{B_r} = \{\boldsymbol{r}_m^{B_r}\}_{m=1}^{p^3}$ from equivalent densities $\{\bar{f}_{qj}^{B_r,B_s}\}$ at equivalent sources $\boldsymbol{C}^{B_s} = \{\boldsymbol{s}_n^{B_s}\}_{n=1}^{p^2}$:

$$\bar{g}_{qj}^{B_r,B_s}(\boldsymbol{r}_m^{B_s}) = \sum_{q=1}^{8}\sum_{n=1}^{P^2} U_{kq}(\boldsymbol{r}_m^{B_r},\boldsymbol{s}_n^{B_s}) \bar{f}_{qj}^{B_r,B_s}(\boldsymbol{s}_n^{B_s}), \tag{88}$$

for $1 \le k, j \le 3$.

4. The **Downward Pass** starts at the level L_r of the receiver tree T_r where the **Upward Pass** has ended and ends at level L of the receiver tree. Meanwhile, the level of the source tree varies from L_s to 0.

   (1) For l from L_r to $L-2$, for each pair $\{B_r, B_s\}$ with B_r traversing all boxes at the level $l+1$ of the receiver tree and B_s traversing all boxes at the level $L-l-1$ of the source tree, interpolate the equivalent fields $\{\bar{g}_{kj}^{B_r,B_s}\}$ at the equivalent sources $\boldsymbol{C}^{B_r} = \{\boldsymbol{r}_m^{B_r}\}_{m=1}^{p^3}$ from the equivalent densities $\{\bar{g}_{kj}^{B_r^p,B_s^c}\}$ at equivalent sources $\boldsymbol{C}^{B_r^p} = \{\boldsymbol{r}_n^{B_r^p}\}_{n=1}^{p^3}$ of all the children clusters of B_s and the parent cluster of B_r:

$$\begin{aligned} &\bar{g}_{kj}^{B_r,B_s}(\boldsymbol{r}_m^{B_r}) = \\ &= \sum_{B_s^c}\sum_{n=1}^{P^3} e^{i\omega\tau(\boldsymbol{r}_m^{B_r};\boldsymbol{s}_c^{B_s^c})} L_{\boldsymbol{C}^{B_r}}(\boldsymbol{r}_m^{B_r};\boldsymbol{r}_n^{B_r^p}) e^{-i\omega\tau(\boldsymbol{r}_n^{B_r^p};\boldsymbol{s}_c^{B_s^c})} \bar{g}_{kj}^{B_r^p,B_s^c}(\boldsymbol{r}_n^{B_r^p}), \end{aligned} \tag{89}$$

   for $1 \le k, j \le 3$, where $\boldsymbol{s}_c^{B_s^c}$ is the center of the receiver box B_s^c.

(2) For each pair $\{B_r, B_s\}$ with B_r traversing all boxes at the leaf level of the receiver tree and B_s traversing all boxes at the root level of the source tree, interpolate equivalent fields $\{\bar{g}_{kj}^{B_r,B_s}\}$ at $\boldsymbol{r} \in B_r \cap \boldsymbol{X}_r$ from the equivalent fields $\{\bar{g}_{kj}^{B_r^p,B_s^c}\}$ at equivalent sources $\boldsymbol{C}^{B_r^p} = \{\boldsymbol{r}_n^{B_r^p}\}_{n=1}^{p^3}$ of all the children level 1 of the source tree and the parent level $L-1$ of the receiver tree:

$$\bar{g}_{kj}^{B_r,B_s}(\boldsymbol{r}) = \sum_{B_s^c} \sum_{n=1}^{P^3} e^{i\omega\tau(\boldsymbol{r};\boldsymbol{s}_c^{B_s^c})} L_{C^{B_r}}(\boldsymbol{r};\boldsymbol{r}_n^{B_r^p}) e^{-i\omega\tau(\boldsymbol{r}_n^{B_r^p};\boldsymbol{s}_c^{B_s^c})} \bar{g}_{kj}^{B_r^p,B_s^c}(\boldsymbol{r}_n^{B_r^p}), \quad (90)$$

for $1 \le k, j \le 3$.

5. **Termination.** For each box B_r at the leaf level of the receiver tree, sum up the equivalent fields over all the boxes of the source tree at the root level, and compute the representative functions g_{kj} at $\boldsymbol{r} \in B_r \cap \boldsymbol{X}_r$ according to equation (73):

$$g_{kj}(\boldsymbol{r}) = \sum_{B_s} \bar{g}_{kj}^{B_r,B_s}(\boldsymbol{r}), \quad \text{for } 1 \le k, j \le 3. \quad (91)$$

To analyze the complexity of the butterfly algorithm, we follow closely the complexity analysis of the butterfly algorithm in [32]. Assume that p Chebyshev nodes are chosen in each dimension and also $O(n) = O(2^L)$ points are sampled in each dimension. Then the total complexity of **Algorithm 2** is

$$O(24p^4n^{5/2} + 72p^5n^{5/2} + 9p^4n^3 + n^3\log n).$$

4.7. Complexity analysis of overall algorithm

In Section 5.3, we see that the overall algorithm consists of two stages. The first stage is preprocessing in which the asymptotic ingredients, such as phase functions, H-B coefficients, and take-off directions for both the S- and P-waves, are computed, and they are further encoded into a set of tables of Chebyshev coefficients. The second stage is post-processing in which globally valid Green's functions are constructed for a given primary source $\boldsymbol{r}_0$ and an arbitrary frequency ω. Since the two stages can be done on different meshes and are independent of each other, we analyze the computational complexities of the two stages separately.

In the following analysis, we will assume that the computational domain is partitioned into $P+1$ layers and P secondary-source planes are set up. In the layer containing the primary source, we just need to compute asymptotic ingredients once. Hence we focus on analyzing the computational complexity of layers in which we need to compute asymptotic ingredients for all the secondary sources on the secondary-source plane and carry out matrix-vector products.

4.7.1. Preprocessing: compute asymptotic ingredients

Since asymptotic ingredients are independent of the frequency ω, we can compute them on very coarse meshes. Moreover, these ingredients are not only continuous away from the source but also continuous with respect to the source itself. Therefore, interpolation not only can be used later to generate asymptotic ingredients on a finer mesh of observation points, but it also can be applied to compute asymptotic ingredients for densely sampled secondary sources.

Assume that the computational domain in the three dimension is uniformly and coarsely discretized by m^3 grid point, which amounts to m sampling points in each dimension. Since the computational domain is partitioned into $P+1$ layers, there are roughly $O(\frac{m^3}{P+1})$ for each layer. And for each plane of the P secondary source planes, m^2 source points are evenly sampled. Then for each secondary source on that plane, we have to compute the asymptotic ingredients in the corresponding layer. According to [32], we can apply higher-order LxF-WENO sweeping methods to compute these asymptotic ingredients for both the S- and P-waves. Thus the computational cost for those asymptotic ingredients at each secondary-source plane is $O(\frac{m^3}{P+1}\log m)$. Totally, there are P secondary-source planes with m^2 sampled points on each plane. Therefore, the overall computational complexity at the total number of m^2P secondary sources is

$$O\left(\frac{m^3}{P+1}\log m \cdot m^2 P\right) = O(m^5 \log m).$$

Although this computational complexity seems to be high, these computed asymptotic ingredients can be stored and reused for different frequencies and different primary sources. And in fact, it is this feature that makes our method appealing to many applications. Also, since the asymptotic ingredients for each secondary source are independent of each other, we can use parallel computing to compute different groups of secondary sources simultaneously. This is analogous to the slowness matching method in [40].

On the other hand, to construct the Green's functions, the whole computational domain is uniformly discretized by n points in each direction. Thus, we need to recover the tables of asymptotic ingredients on roughly $O(\frac{n^3}{P+1})$ points in each layer for some specified secondary sources. And this requires complexity of $O(\frac{n^3}{P+1})$ for each layer and each secondary source; see details in [32].

4.7.2. Postprocessing: construct global Green's tensors

Given a primary source $\boldsymbol{r}_0$ and a frequency parameter ω, a fine mesh is required to capture highly oscillatory Green's functions. To estimate the needed mesh points in each direction, first we need to approximate the minimum wavelength for both S- and P-waves according to the given slownesses and frequency so that the total number of waves can be estimated. Then we need to sample 4-6 points per wave in order to capture the oscillations. Certainly, it does not hurt to take more points per wavelength. Hence the total number of mesh points can be chosen to satisfy the above consideration, and it is assumed to be $N = n^3$ with n points in each direction. Correspondingly, the number of points on each secondary-source plane can be chosen to be roughly n^2 with n points in each direction.

Once those asymptotic ingredients are available on this specified mesh inside each layer, the Green's functions can be constructed by the butterfly algorithm. Given the accuracy $\epsilon > 0$, according to [7], we may choose $p = p_\epsilon < O(\log^2(\frac{1}{\epsilon}))$ for the order of the one-dimension Chebyshev nodes in the butterfly algorithm so that the algorithm for computing the summation achieves the accuracy ϵ in $O(\frac{N}{P+1}\log N)$ in each layer, where the prefactor depends only on ϵ and is independent of ω. Therefore, the overall complexity of constructing the Green's function by the butterfly algorithm in P layers is $O(\frac{P}{P+1}N\log N) = O(N\log N)$ for a given primary source and a given frequency. To speed up the construction, we use the "build-in" parfor (parallel for) loop in our MATLAB implementation; see details in [32].

5. Numerical examples

In the following examples, we first compute the asymptotic ingredients, phase functions, H-B coefficients, and take-off directions for both S- and P-waves on a coarse mesh of the region enclosing the primary source. When the corresponding mesh size is used for computing the asymptotic ingredients at secondary sources, the coarse mesh will be restricted to a neighborhood of each secondary source. The asymptotic ingredients are compressed into tables of Chebyshev coefficients. Thus for all numerical experiments, the asymptotic ingredients are given as compressed data, and they are recovered onto the finer mesh by the Chebyshev partial summation when needed. The computational domain for constructing wave fields is discretized into mesh points with roughly 5 points per wavelength in each direction.

Unless otherwise stated, all computations were executed in a 20-core Intel Xeon processor with 377 GBytes of RAM associated with a bi-processor Intel Xeon Gold 6148 node at the High Performance Computing Center (HPCC) of MSU. All the computations in Stage 1 were carried out in parallel for all secondary sources, while the butterfly algorithm in Stage 2 was carried out in parallel in 10 cores as well.

When the elastic parameters are not constants, the exact solutions of the Green's functions are not available. Thus, to validate our method, we obtain reference solutions by applying the FDTD method [41] directly to time-domain elastic wave equations. However, due to limited computing resources, we are only able to compute the FDTD-based solutions at low frequencies, so that the related comparisons will be only carried out at these low frequencies.

Example 1: A constant model. In this example, we take $\rho = 1$, $\lambda = 1$, and $\mu = 1$. The computational setup for our asymptotic method is the following.

- The computational domain is $[0,2]\times[0,2]\times[0,2]$.
- The coarse mesh size is $51\times51\times51$ with grid size $h = 0.04$.
- The source point is $(1.0, 1.0, 0.2)^T$.
- The computational domain is partitioned in the following way: the first layer containing the primary source is $\Omega_1 = [0,2]\times[0,2]\times[0,1.4]$, and one secondary source plane is placed at $z = 1.2$. We coarsely sample 51×51 equally spaced secondary sources on the truncated source domain $S_1 = [0,2]\times[0,2]\times\{z = 1.2\}$; then the corresponding receiver domain is $\Omega_2 = [0,2]\times[0,2]\times[1.4,2]$, which is $d_f = 0.2$ vertically away from the secondary source plane S_1.

In this example, since all elastic parameters are constants, we use the exact solutions to check the accuracy of our numerical solutions. Five points per wavelength are chosen in the butterfly algorithm in Stage 2 to capture highly oscillatory waves. In Table 5.1, we compute the L_∞ error between the numerical solutions of our method, denoted as $\boldsymbol{G}_{num}$, and the exact solutions, denoted as $\boldsymbol{G}_{exa}$, for the total nine elements of $\boldsymbol{G}(\boldsymbol{r};\boldsymbol{r}_0)$ in Ω_2,

$$E_\infty = ||\boldsymbol{G}_{num} - \boldsymbol{G}_{exa}||_\infty. \tag{92}$$

Mesh in Ω_2	$31\times 31\times 11$	$61\times 61\times 21$	$121\times 121\times 41$	$241\times 241\times 81$
ω	6π	12π	24π	48π
NPW	5	5	5	5
E_∞ $(p=9)$	3.18E-2	2.87E-2	3.46E-2	5.34E-2
E_∞ $(p=11)$	3.18E-2	2.52E-2	1.48E-2	2.75E-2
E_∞ $(p=13)$	3.19E-2	2.47E-2	1.18E-2	9.1E-3

Table 5.1: Example 1 with constant elastic parameters. L_∞-norm errors between the numerical solutions of our fast Huygens sweeping method and the exact solutions. ω: the frequency parameter; NPW: the number of points per wavelength; p: the number of Chebyshev order used in each dimension; E_∞: The L_∞-norm errors between solutions by the two different approaches.

Mesh in Ω_2	$31\times 31\times 11$	$61\times 61\times 21$	$121\times 121\times 41$	$241\times 241\times 81$
ω	6π	12π	24π	48π
NPW	5	5	5	5
$T_M(p=9)$	57.71	129.35	551.73	3393.2
$T_M(p=11)$	74.36	195.0	927.02	5452.7
$T_M(p=13)$	75.47	219.62	1414.6	8206.6

Table 5.2: Example 1 with constant elastic parameters. Computational time using the butterfly algorithm. ω: the frequency parameter; NPW: the number of points per wavelength; T_M (unit: s): the CPU time for the construction of total nine elements of the Green's function for the S-wave in the receiver domain Ω_2 by the butterfly algorithm; p: the Chebyshev order used in each dimension.

The errors are obtained for different frequency ω and different Chebyshev order p used in each dimension. Our numerical solutions are of accuracy $O(1/\omega)$ as expected. Table 5.2 lists running times of the butterfly algorithm for computing all nine elements of $\boldsymbol{G}(\boldsymbol{r};\boldsymbol{r}_0)$ in Ω_2. The computational time is consistent with the computational complexity $O(N\log N)$ as analyzed above, where N is the total number of mesh points in Ω_2.

Figures 5.1, 5.2 and 5.3 show the comparison between the numerical solution by our Huygens sweeping method with the Chebyshev order $p=13$ and the exact solution at frequency $\omega=24\pi$. We can see that our solutions match with the exact solutions very well.

Example 2: A Gaussian model. We take $\lambda=1$ and $\mu=1$ but variable ρ:

$$\rho = 9.0\left(3.0 - 1.75e^{-\frac{(x-1)^2+(y-1)^2+(z-1)^2}{0.64}}\right)^{-2}.$$

In this case, the exact solution is not available, so we compute the FDTD-based solutions as reference solutions to check the accuracy of our method.

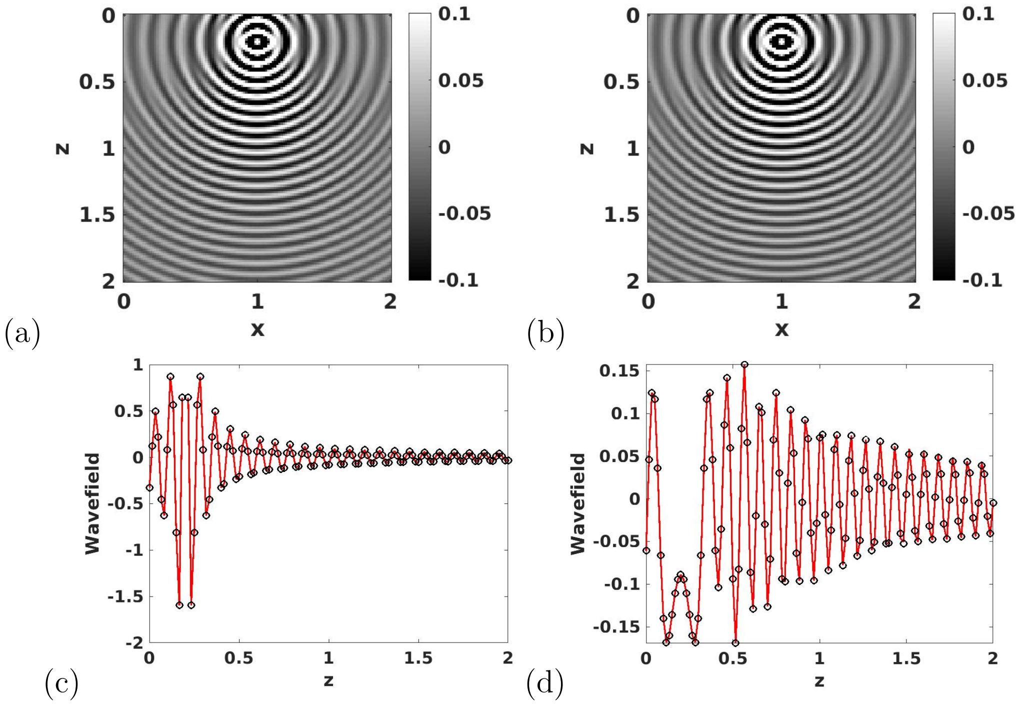

Figure 5.1: Example 1 with $\boldsymbol{r}_0 = (1.0, 1.0, 0.2)^T$ and $\omega = 24\pi$. The real part of the xx-component of $\boldsymbol{G}(\boldsymbol{r}; \boldsymbol{r}_0)$ at $y = 1.0$ computed via (a) the Huygens sweeping method with $p = 13$; (b) the exact solution. The detailed comparison of the real part of the xx-component of $\boldsymbol{G}(\boldsymbol{r}; \boldsymbol{r}_0)$ at (c): line $x = 1.0$ and $y = 1.0$ and (d): line $x = 0.8$ and $y = 1.0$. Red solid line: the exact solution. Black circle: the Huygens sweeping solution. Mesh: $121 \times 121 \times 121$.

The computational setup for our asymptotic method is as follows.

- The computational domain is $\Omega = [0, 2] \times [0, 2] \times [0, 2]$.
- The coarse mesh size is $51 \times 51 \times 51$ with grid size $h = 0.04$.
- The source point is $(1.0, 1.0, 0.2)^T$.
- The computational domain is partitioned as follows: the first layer containing the primary source is $\Omega_1 = [0, 2] \times [0, 2] \times [0, 1.4]$, and one secondary source plane is placed at $z = 1.2$. We coarsely sample 51×51 equally spaced secondary sources on the truncated source domain $S_1 = [0, 2] \times [0, 2] \times \{z = 1.2\}$; then the corresponding receiver domain is $\Omega_2 = [0, 2] \times [0, 2] \times [1.4, 2]$, which is $d_f = 0.2$ vertically away from the secondary source plane S_1.

We use roughly 5 points per wavelength in Stage 2. Table 5.3 records the running times for constructing the Green's functions $\boldsymbol{G}(\boldsymbol{r}, \boldsymbol{r}_0)$ in Ω_2 using the fast Huygens sweeping method. Different Chebyshev orders are used in each dimension. We can see that as the mesh points are doubled in each dimension, the running time increases by about six times. Figure 5.4 shows the comparison of numerical solutions of the real part of the xx-component of the Green's function computed by two different methods at frequency $\omega = 10\pi$: the butterfly-algorithm based Huygens sweeping method with order $p = 13$ and the FDTD method. The comparisons of numerical solutions for the zz-components of the Green's functions by these two methods are shown in Figure 5.5.

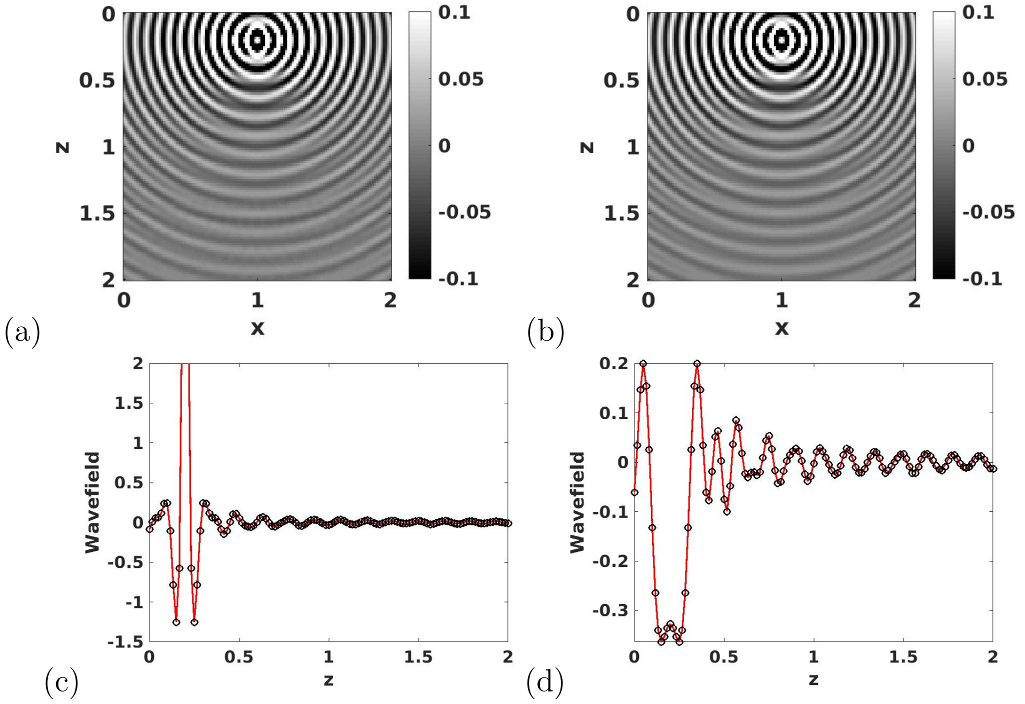

Figure 5.2: Example 1 with $\boldsymbol{r}_0 = (1.0, 1.0, 0.2)^T$ and $\omega = 24\pi$. The real part of the zz-component of $\boldsymbol{G}(\boldsymbol{r}; \boldsymbol{r}_0)$ at $y = 1.0$ computed via (a) the Huygens sweeping method with $p = 13$; (b) the exact solution. The detailed comparison of the real part of the zz-component of $\boldsymbol{G}(\boldsymbol{r}; \boldsymbol{r}_0)$ at (c): line $x = 1.0$ and $y = 1.0$ and (d): line $x = 0.8$ and $y = 1.0$. Red solid line: the exact solution; black circle: the Huygens sweeping solution. Mesh: 121 × 121 × 121.

In addition, we construct the Green's functions at $\omega = 20\pi$ as shown in Figure 5.6 by the fast Huygens sweeping method. At this frequency, the FDTD method requires very fine meshes so that it is very time-consuming and resource-demanding for the FDTD to compute a numerical solution, and thus we are not able to show the corresponding FDTD result here.

Mesh in Ω_2	$61 \times 61 \times 21$	$121 \times 121 \times 41$	$241 \times 241 \times 81$	$337 \times 337 \times 105$
ω	5π	10π	20π	$80/3\pi$
NPW	5	5	5	5
$T_M(p = 9)$	176.89	649.35	3716.7	4058.7
$T_M(p = 11)$	264.23	1205.3	6168.0	7460.5
$T_M(p = 13)$	220.84	1369.0	7931.5	8174.2

Table 5.3: Example 2: the Gaussian model. Computational times using the butterfly algorithm. ω: the frequency parameter; NPW: the number of points per wavelength; T_M (unit: s): the CPU time for the construction of the nine elements of the Green's function for the S-wave in the receiver domain Ω_2 by the butterfly algorithm; p: the Chebyshev order used in each dimension.

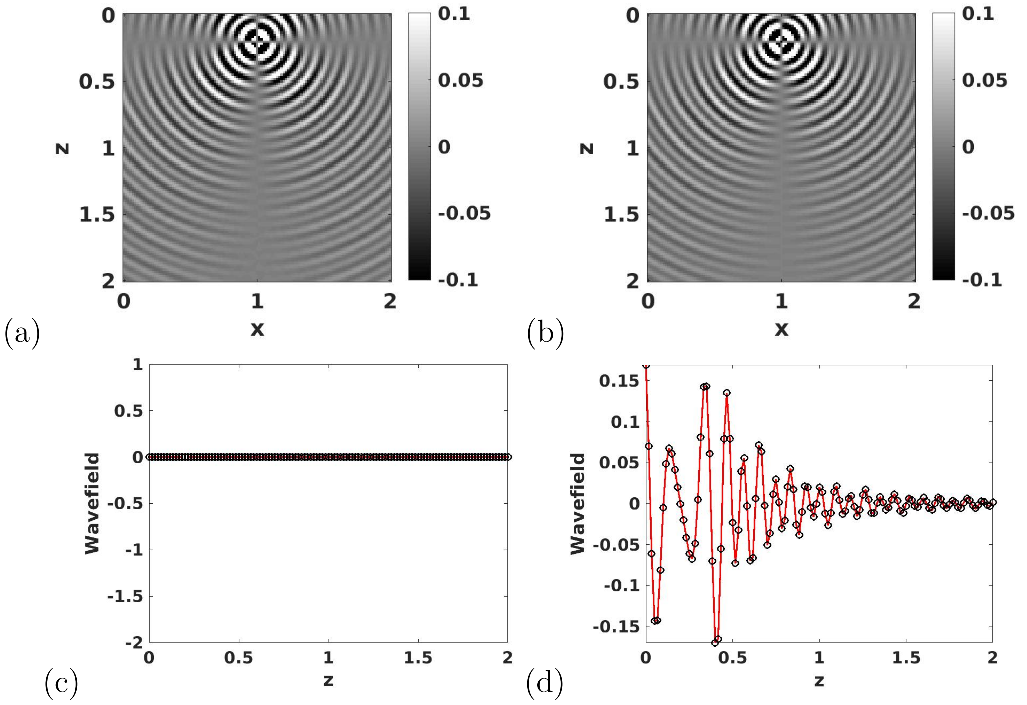

Figure 5.3: Example 1 with $\boldsymbol{r}_0 = (1.0, 1.0, 0.2)^T$ and $\omega = 24\pi$. The real part of the xz-component of $\boldsymbol{G}(\boldsymbol{r}; \boldsymbol{r}_0)$ at $y = 1.0$ computed via (a) the Huygens sweeping method with $p = 13$; (b) the exact solution. The detailed comparison of the real part of the xz-component of $\boldsymbol{G}(\boldsymbol{r}; \boldsymbol{r}_0)$ at (c): line $x = 1.0$ and $y = 1.0$ and (d): line $x = 0.8$ and $y = 1.0$. Red solid line: the exact solution. Black circle: the Huygens sweeping solution. Mesh: $121 \times 121 \times 121$.

Example 3: A Gaussian model. We take $\rho = 9$ but variable λ and μ. Here we set $\lambda = \mu$ and

$$\mu = (3.0 - 1.75e^{-\frac{(x-1.0)^2+(y-1)^2+(z-1)^2}{0.64}})^2.$$

In this example, we compute the FDTD-based solution to check the accuracy of our method.

The computational setup for our asymptotic method is as the following.

- The computational domain is $\Omega = [0, 2] \times [0, 2] \times [0, 2]$.
- The coarse mesh size is $51 \times 51 \times 51$ with grid size $h = 0.04$.
- The source point is $(0.8, 1.0, 0.2)^T$.
- The computational domain is partitioned as follows: the first layer containing the primary source is $\Omega_1 = [0, 2] \times [0, 2] \times [0, 1.4]$, and one secondary source plane is placed at $z = 1.2$. We coarsely sample 51×51 equally spaced secondary sources on the truncated source domain $S_1 = [0, 2] \times [0, 2] \times \{z = 1.2\}$; then the corresponding receiver domain is $\Omega_2 = [0, 2] \times [0, 2] \times [1.4, 2]$, which is $d_f = 0.2$ vertically away from the secondary source plane S_1.

We use four points per wavelength to capture the wave in the butterfly algorithm. Figure 5.7, 5.8, and 5.9 show the comparisons of numerical solutions of the real part of the xx-, zz-, and xz- components of the Green's functions computed by two different methods at frequency $\omega = 12\pi$: the Huygens sweeping method with order $p = 13$ and the FDTD method. The numerical solutions of the Huygens sweeping method are consistent with the FDTD solutions.

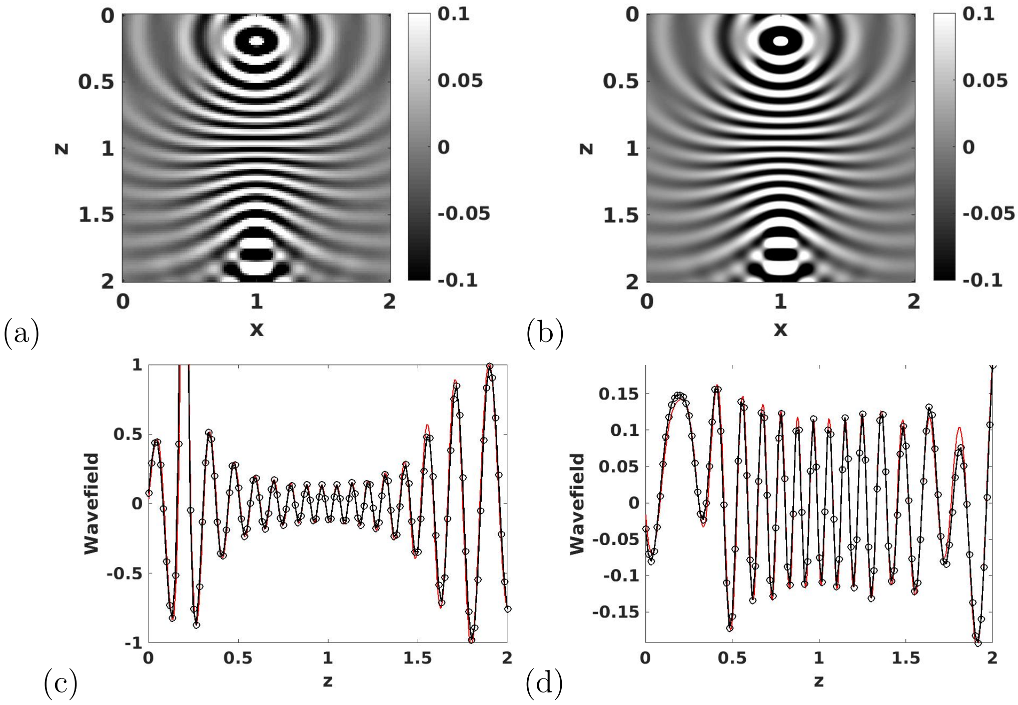

Figure 5.4: Example 2 with $\boldsymbol{r}_0 = (1.0, 1.0, 0.2)^T$ and $\omega = 10\pi$. The real part of the xx-component of $\boldsymbol{G}(\boldsymbol{r}; \boldsymbol{r}_0)$ at $y = 1.0$ computed via (a) the Huygens sweeping method with $p = 13$; (b) the FDTD method.
The detailed comparison of the real part of the xx-component of $\boldsymbol{G}(\boldsymbol{r}; \boldsymbol{r}_0)$ at (c): line $x = 1.0$ and $y = 1.0$ and (d): line $x = 0.8$ and $y = 1.0$. Red solid line: the FDTD solution. Black circled line: the solution by the Huygens sweeping method. Mesh in (a): $121 \times 121 \times 121$; mesh in (b): $401 \times 401 \times 401$.

Example 4: A waveguide model. We take $\rho = 1$ but variable λ and μ. Here we set $\lambda = \mu$ and

$$\mu = \left(1.0 - 0.5e^{-6((x-1)^2+(y-1)^2)}\right)^2.$$

In this example, we have the following setup.

- The computational domain is $\Omega = [0, 2] \times [0, 2] \times [0, 1.6]$.
- The coarse mesh size is $51 \times 51 \times 41$ with grid size $h = 0.04$.
- The source point is $(1.0, 1.0, 0.2)^T$ or $(0.8, 1.0, 0.12)^T$.
- The computational domain is partitioned as follows: the first layer containing the primary source is $\Omega_1 = [0, 2] \times [0, 2] \times [0, 0.8]$, and two secondary source planes are placed at $z = 0.6$ and $z = 1.0$, respectively. We coarsely sample 51×51 equally spaced secondary sources on the truncated source domains

$$S_1 = [0, 2] \times [0, 2] \times \{z = 0.6\} \quad \text{and} \quad S_2 = [0, 2] \times [0, 2] \times \{z = 1.0\};$$

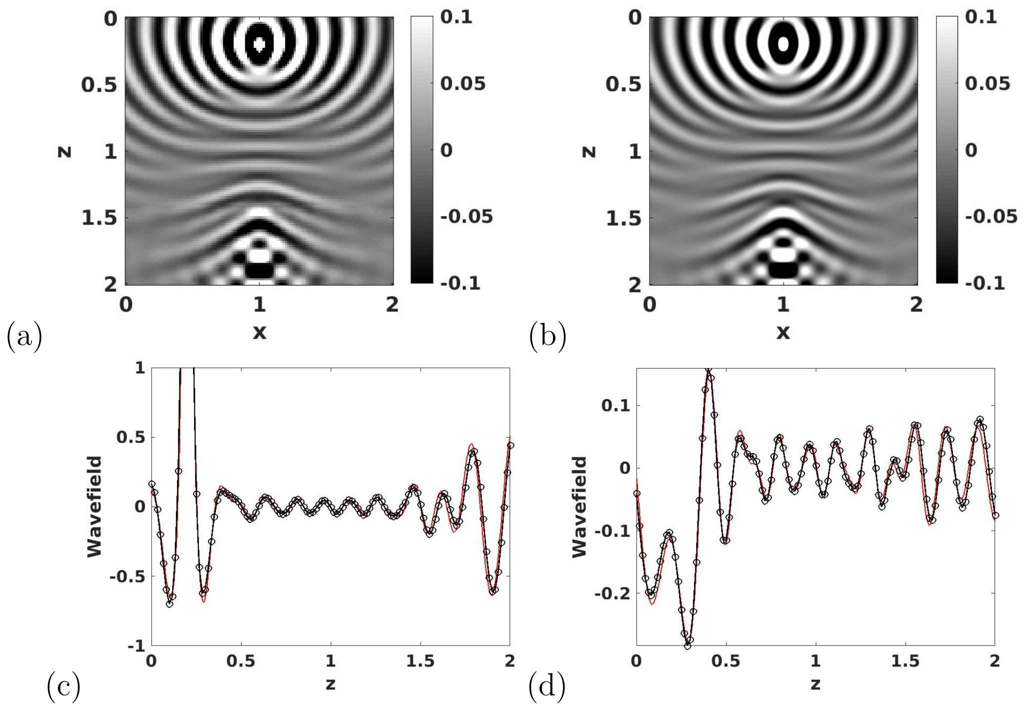

Figure 5.5: Example 2 with $\boldsymbol{r}_0 = (1.0, 1.0, 0.2)^T$ and $\omega = 10\pi$. The real part of the zz-component of $\boldsymbol{G}(\boldsymbol{r};\boldsymbol{r}_0)$ at $y = 1.0$ computed via (a) the Huygens sweeping method with $p = 13$; (b) the FDTD solution.
The detailed comparison of the real part of the zz-component of $\boldsymbol{G}(\boldsymbol{r};\boldsymbol{r}_0)$ at (c): line $x = 1.0$ and $y = 1.0$ and (d): line $x = 0.8$ and $y = 1.0$. Red solid line: FDTD solution. Black circled line: the solution by the Huygens sweeping method. Mesh in (a): $121 \times 121 \times 121$; mesh in (b): $401 \times 401 \times 401$.

then the corresponding receiver domains are

$$\Omega_2 = [0, 2] \times [0, 2] \times [0.8, 1.2] \quad \text{and} \quad \Omega_3 = [0, 2] \times [0, 2] \times [1.2, 1.6]$$

which are $d_f = 0.2$ vertically away from the secondary source planes S_1 and S_2, respectively.

The exact solution for this example is not available, so we use the FDTD method to obtain a reference solution. Approximately 5 points per wavelength is used in the butterfly algorithm. First, we construct the numerical solutions of the Green's function at the source $(1.0, 1.0, 0.2)^T$ and at frequency $\omega = 10\pi$ by the fast Huygens sweeping method with order $p = 13$. The comparisons with the FDTD solutions of the xx- and zz- components of the Green's functions are shown in Figures 5.10 and 5.11, respectively.

Next, we use the same data tables for all secondary sources to compute the Green's functions in the receiver domain Ω_2 and Ω_3 for a different source $(0.8, 1.0, 0.2)^T$ and different frequency $\omega = 12\pi$. The comparisons between the solution of our method and the FDTD solution are given in Figure 6.1. The numerical solutions of our method are consistent with the FDTD solutions.

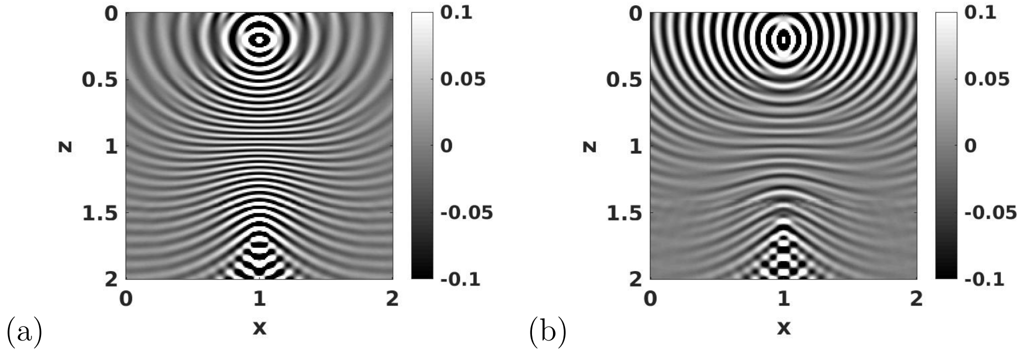

(a) (b)

Figure 5.6: Example 2 with $\boldsymbol{r}_0 = (1.0, 1.0, 0.2)^T$ and $\omega = 20\pi$. The real part of the (a) xx- and (b) zz-component of $\boldsymbol{G}(\boldsymbol{r}; \boldsymbol{r}_0)$ at $y = 1.0$ computed by the Huygens sweeping method with $p = 13$. Mesh: 241 × 241 × 241.

In addition, we construct the Green's functions at higher frequency $\omega = 20\pi$ as shown in Figure 6.2 by the Huygens sweeping method.

6. Conclusion

Starting from the truncated Hadamard-Babich ansatz, we have developed a new fast Huygens sweeping method for computing the globally valid asymptotic Green's functions of elastic wave equations in an inhomogeneous medium in the high frequency regime and in the presence of caustics. The new method uses the Huygens-Kirchhoff integral to integrate many locally valid asymptotic Green's functions into a globally valid asymptotic Green's function so that caustics can be treated automatically. To accelerate matrix-vector products induced by the Huygens-Kirchhoff integral, we have used the butterfly algorithm to speed up the multiplication process with optimal complexity. Numerical examples demonstrate the performance, efficiency, and accuracy of our new method.

References

[1] G. S. Avila, J. B. Keller: *The high-frequency asymptotic field of a point source in an inhomogeneous medium*, Commun. Pure Appl. Math. 16 (1963) 363–381.

[2] V. M. Babich: *The short wave asymptotic form of the solution for the problem of a point source in an inhomogeneous medium*, USSR Comp. Math. Math. Physics 5/5 (1965) 247–251.

[3] V. M. Babich: *A point source of electromagnetic waves in an inhomogeneous medium: a high frequency ansatz and the dual nonstationary singular solution*, J. Math. Sciences 243/5 (2019) 634–639.

[4] I. M. Babuška, S. A. Sauter: *Is the pollution effect of the FEM avoidable for the Helmholtz equation considering high wave numbers?*, SIAM Review 42 (2000) 451–484.

[5] A. Bayliss, C. I. Goldstein, E. Turkel: *On accuracy conditions for the numerical computation of waves*, J. Comput. Phys. 59 (1985) 396–404.

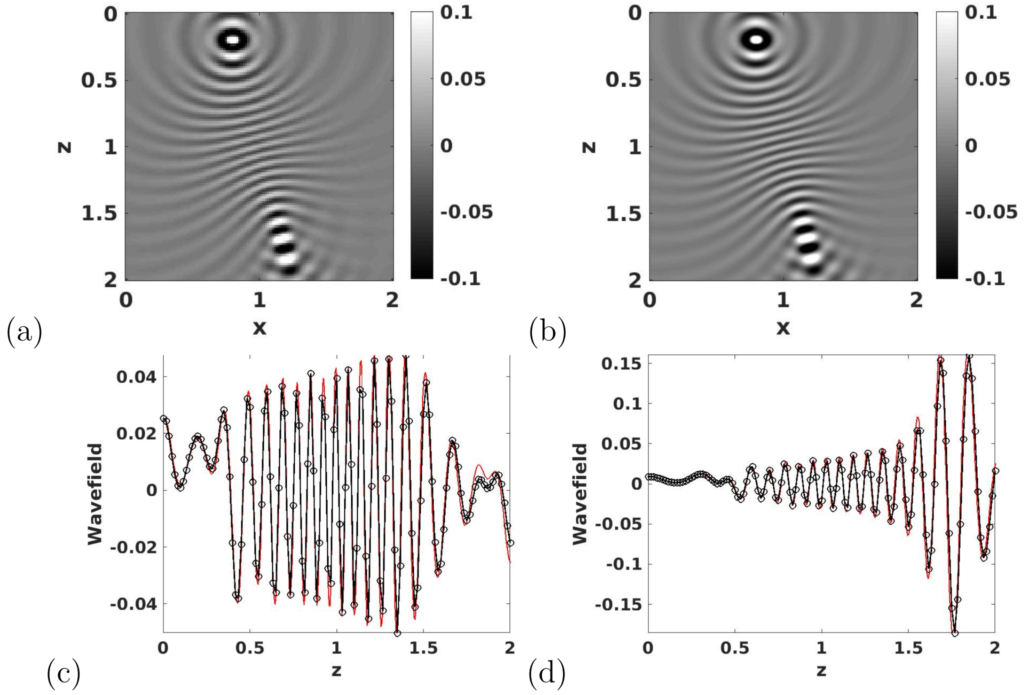

Figure 5.7: Example 3 with $\boldsymbol{r}_0 = (0.8, 1.0, 0.2)^T$ and $\omega = 12\pi$. The real part of the xx-component of $\boldsymbol{G}(\boldsymbol{r};\boldsymbol{r}_0)$ at $y = 1.0$ computed via (a) the Huygens sweeping method with $p = 13$ and (b) the FDTD method.
The detailed comparison of the real part of the xx-component of $\boldsymbol{G}(\boldsymbol{r};\boldsymbol{r}_0)$ at (c): line $x = 1.0$ and $y = 1.0$ and (d): line $x = 1.2$ and $y = 1.0$. Red solid line: the FDTD solution. Black circled line: the solution of the Huygens sweeping method. Mesh in (a): $121 \times 121 \times 121$; mesh in (b): $401 \times 401 \times 401$.

[6] J. P. Boyd: *Chebyshev and Fourier Spectral Methods*, 2nd ed., Dover, New York (2001).

[7] E. Candes, L. Demanet, L. Ying: *A Fast Butterfly Algorithm for the computation of Fourier integral operators*, SIAM Multiscale Model. Simul. 7 (2009) 1727–1750.

[8] B. Engquist, H.-K. Zhao: *Approximate separability of the Green's function of the Helmholtz equation in the high-frequency limit*, Comm. Pure Appl. Math. 71 (2018) 2220–2274.

[9] J. Fang, J. Qian, L. Zepeda-Nunez, H. Zhao: *A hybrid approach to solve the high-frequency Helmholtz equation with source singularity in inhomogeneous media*, J. Comput. Phys. 371 (2018) 261–279.

[10] S. Fomel, S. Luo, H. K. Zhao: *Fast sweeping method for the factored eikonal equation*, J. Comput. Phys. 228 (2009) 6440–6455.

[11] I. M. Gelfand, G. E. Shilov: *Generalized Functions, Volume 1*, Academic Press, New York (1964).

[12] G. S. Jiang, D. Peng: *Weighted ENO schemes for Hamilton-Jacobi equations*, SIAM J. Sci. Comput. 21 (2000) 2126–2143.

[13] G. S. Jiang, C. W. Shu: *Efficient implementation of weighted ENO schemes*, J. Comput. Phys. 126 (1996) 202–228.

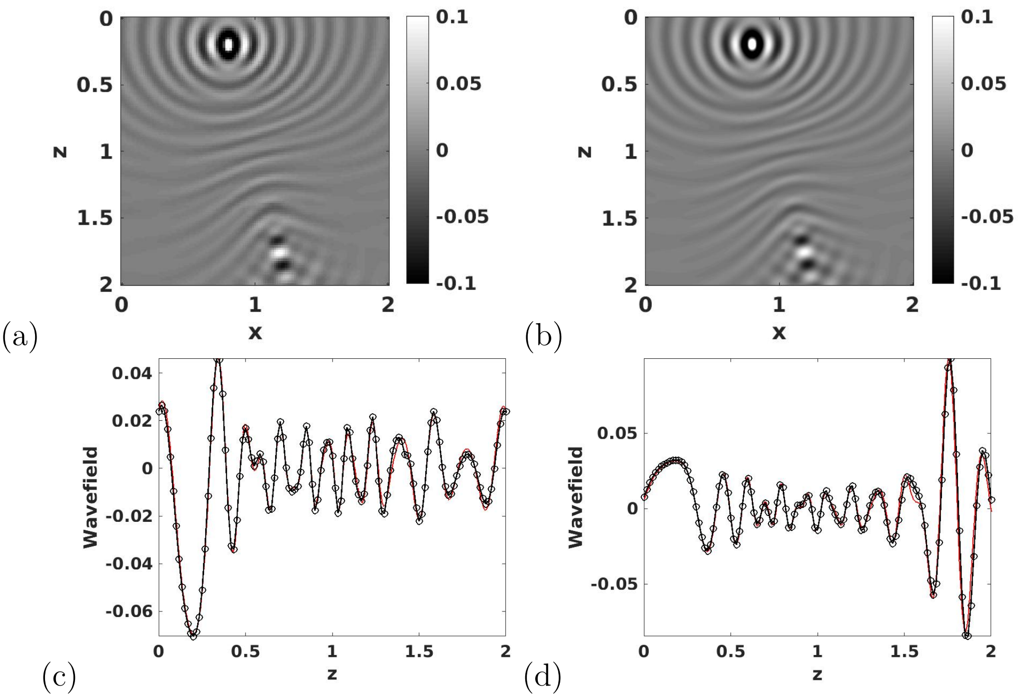

(a) (b)

(c) (d)

Figure 5.8: Example 3 with $\boldsymbol{r}_0 = (0.8, 1.0, 0.2)^T$ and $\omega = 12\pi$. The real part of the zz-component of $\boldsymbol{G}(\boldsymbol{r}; \boldsymbol{r}_0)$ at $y = 1.0$ computed via (a) the Huygens sweeping method with $p = 13$ and (b) the FDTD method.
The detailed comparison of the real part of the zz-component of $\boldsymbol{G}(\boldsymbol{r}; \boldsymbol{r}_0)$ at (c): line $x = 1.0$ and $y = 1.0$ and (d): line $x = 1.2$ and $y = 1.0$. Red solid line: the FDTD solution. Black circled line: the solution of the Huygens sweeping method. Mesh in (a): $121 \times 121 \times 121$; mesh in (b): $401 \times 401 \times 401$.

[14] C. Y. Kao, S. J. Osher, J. Qian: *Lax-Friedrichs sweeping schemes for static Hamilton-Jacobi equations*, J. Comput. Phys. 196 (2004) 367–391.

[15] F. C. Karal Jr., J. B. Keller: *Elastic wave propagation in homogeneous and inhomogeneous media*, J. Acoust. Soc. Amer. 31/6 (1959) 694–705.

[16] V. D. Kupradze, T. G. Gegelia, M. O. Basheleishvili, T. V. Burchuladze: *Three-Dimensional Problems of the Mathematical Theory of Elasticity and Thermoelasticity*, North-Holland, Amsterdam (1979).

[17] W. Kwan, S. Leung, X.-P. Wang, J. Qian: *A fast Huygens sweeping method for capturing paraxial multi-color optical self-focusing in nematic liquid crystals*, J. Comput. Physics 348 (2017) 108–138.

[18] S. Leung, J. Qian: *The backward phase flow and FBI-transform-based Eulerian Gaussian beams for the Schrödinger equation*, J. Comput. Phys. 229 (2010) 8888–8917.

[19] S. Leung, J. Qian, S. Serna: *Fast Huygens sweeping methods for Schroedinger equations in the semiclassical regime*, Methods Appl. Analysis 21 (2014) 31–66.

[20] W. Li, J. Qian: *Newton-type Gauss-Seidel Lax-Friedrichs high-order fast sweeping methods for solving generalized eikonal equations at large-scale discretization*, Comp. Math. Appl. 79 (2020) 1222–1239.

[21] X. D. Liu, S. J. Osher, T. Chan: *Weighted essentially nonoscillatory schemes*, J. Comput. Phys. 115 (1994) 200–212.

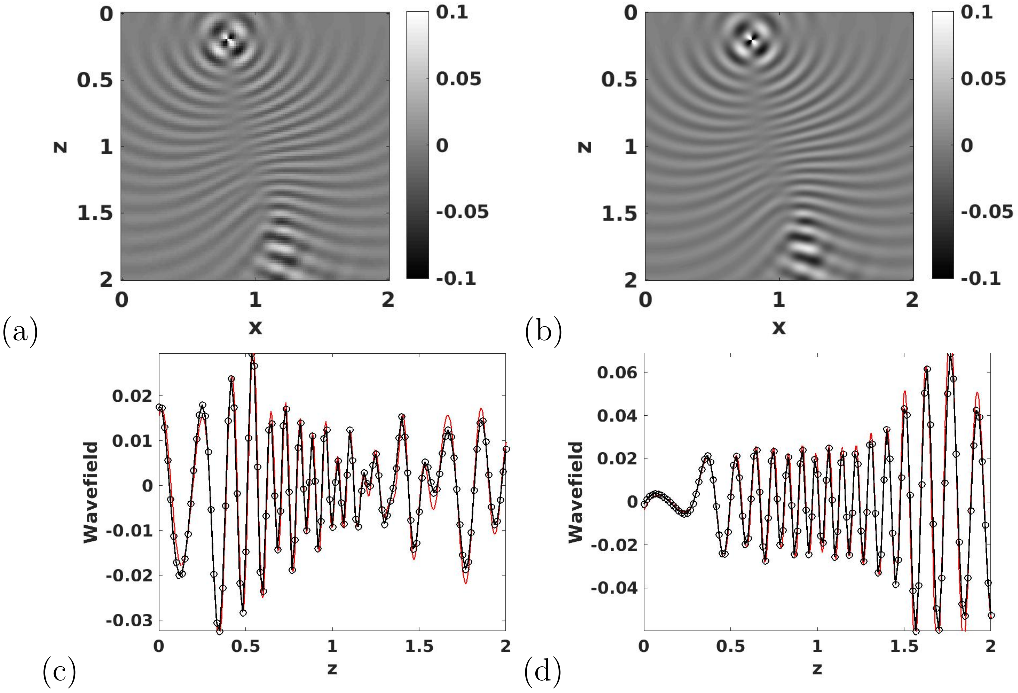

(a) (b) (c) (d)

Figure 5.9: Example 3 with $\boldsymbol{r}_0 = (0.8, 1.0, 0.2)^T$ and $\omega = 12\pi$. The real part of the xz-component of $\boldsymbol{G}(\boldsymbol{r}; \boldsymbol{r}_0)$ at $y = 1.0$ computed via (a) the Huygens sweeping method with $p = 13$ and (b) the FDTD method.
The detailed comparison of the real part of the xz-component of $\boldsymbol{G}(\boldsymbol{r}; \boldsymbol{r}_0)$ at (c): line $x = 1.0$ and $y = 1.0$ and (d): line $x = 1.2$ and $y = 1.0$. Red solid line: the FDTD solution. Black circled line: the solution of the Huygens sweeping method. Mesh in (a): $121 \times 121 \times 121$; mesh in (b): $401 \times 401 \times 401$.

[22] W. Lu, J. Qian, R. Burridge: *Babich-like ansatz for three-dimensional point-source Maxwell's equations in an inhomogeneous medium at high frequencies*, SIAM J. Multiscale Model. Simul. 14/3 (2016) 1089–1122.

[23] W. Lu, J. Qian, R. Burridge: *Babich's expansion and the fast Huygens sweeping method for the Helmholtz wave equation at high frequencies*, J. Comput. Phys. 313 (2016) 478–510.

[24] W. Lu, J. Qian, R. Burridge: *Extending Babich's ansatz for point-source Maxwell's equations using Hadamard's method*, SIAM J. Multiscale Model. Simul. 16 (2018) 727–751.

[25] S. Luo, J. Qian: *Fast sweeping methods for factored anisotropic eikonal equations: multiplicative and additive factors*, J. Sci. Comput. 52 (2012) 360–382.

[26] S. Luo, J. Qian, R. Burridge: *Fast Huygens sweeping methods for Helmholtz equations in inhomogeneous media in the high frequency regime*, J. Comput. Phys. 270 (2014) 378–401.

[27] S. Luo, J. Qian, R. Burridge: *High-order factorization based High-order hybrid fast sweeping methods for point-source eikonal equations*, SIAM J. Numer. Analysis 52 (2014) 23–44.

[28] E. Michielssen, A. Boag: *A multilevel matrix decomposition algorithm for analysing scattering from large structures*, IEEE Trans. Antennas Propagation 44/8 (1996) 1086–1093.

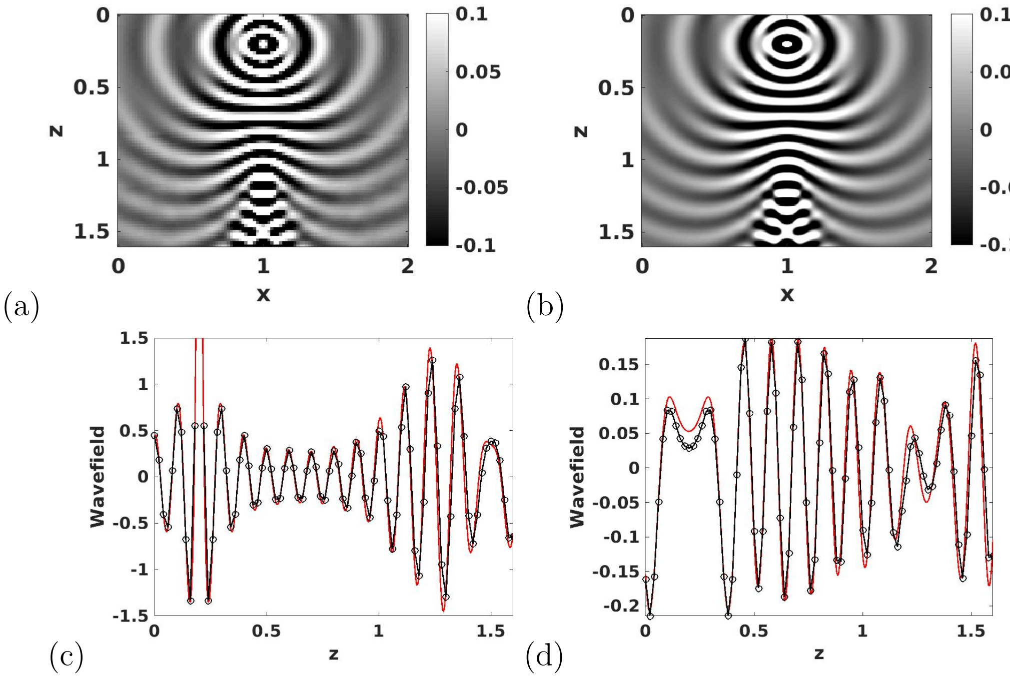

Figure 5.10: Example 4 with $\boldsymbol{r}_0 = (1.0, 1.0, 0.2)^T$ and $\omega = 10\pi$. The real part of the xx-component of $\boldsymbol{G}(\boldsymbol{r}; \boldsymbol{r}_0)$ at $y = 1.0$ computed via (a) the Huygens sweeping method with $p = 13$ and (b) the FDTD method.
The detailed comparison of the real part of the xx-component of $\boldsymbol{G}(\boldsymbol{r}; \boldsymbol{r}_0)$ at (c): line $x = 1.0$ and $y = 1.0$ and (d): line $x = 0.8$ and $y = 1.0$. Red solid line: the FDTD solution. Black circled line: the solution of the Huygens sweeping method. Mesh in (a): $101 \times 101 \times 81$; mesh in (b): $401 \times 401 \times 321$.

[29] M. O'Neil, V. Rokhlin: *A new class of analysis-based fast transforms*, Tech. Report 1384, Dept. of Computer Science, Yale University, New Haven (2007).

[30] S. J. Osher, C. W. Shu: *High-order essentially non-oscillatory schemes for Hamilton-Jacobi equations*, SIAM J. Numer. Analysis 28 (1991) 907–922.

[31] A. Pica: *Fast and accurate finite-difference solutions of the 3-D eikonal equation parameterized in celerity*, in: SEG Annual Meeting, Dallas, Texas (1997) 1774–1777.

[32] J. Qian, W. Lu, L. Yuan, S. Luo, R. Burridge: *Eulerian geometrical optics and fast Huygens sweeping methods for three-dimensional time-harmonic high-frequency Maxwell's equations in inhomogeneous media*, SIAM J. Multiscale Model. Simul. 16 (2016) 595–636.

[33] J. Qian, S. Luo, R. Burridge: *Fast Huygens sweeping methods for multi-arrival Green's functions of Helmholtz equations in the high frequency regime*, Geophysics 80 (2015) T91–T100.

[34] J. Qian, J. Song, W. Lu, R. Burridge: *Hadamard-Babich ansatz for point-source elastic wave equations in variable media at high frequencies*, SIAM Multiscale Model. Simul. 19 (2021) 46–86.

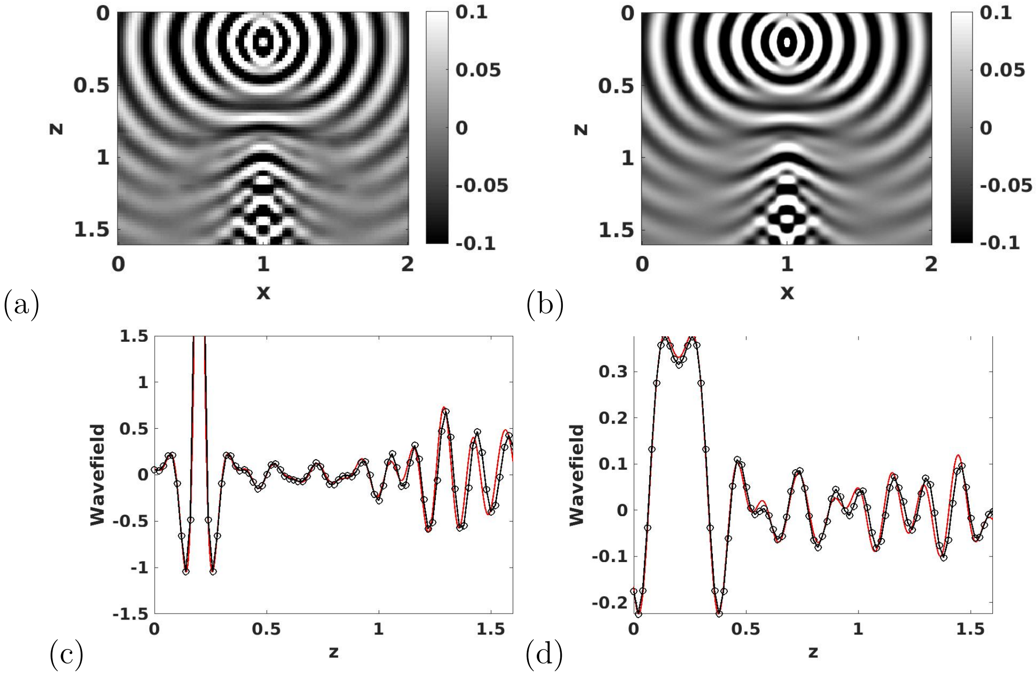

Figure 5.11: Example 4 with $\boldsymbol{r}_0 = (1.0, 1.0, 0.2)^T$ and $\omega = 10\pi$. The real part of the zz-component of $\boldsymbol{G}(\boldsymbol{r};\boldsymbol{r}_0)$ at $y = 1.0$ computed via (a) the Huygens sweeping method with $p = 13$ and (b) the FDTD method.
The detailed comparisons of the real part of the zz-component of $\boldsymbol{G}(\boldsymbol{r};\boldsymbol{r}_0)$ at (c): line $x = 1.0$ and $y = 1.0$ and (d): line $x = 0.8$ and $y = 1.0$. Red solid line: FDTD solution. Black circled line: the solution of the Huygens sweeping method. Mesh in (a): $101 \times 101 \times 81$; mesh in (b): $401 \times 401 \times 321$.

[35] J. Qian, W. W. Symes: *Adaptive finite difference method for traveltime and amplitude*, Geophysics 67 (2002) 167–176.

[36] J. Qian, L. Ying: *Fast Gaussian wavepacket transforms and Gaussian beams for the Schrödinger equation*, J. Comput. Phys. 229 (2010) 7848–7873.

[37] J. Qian, L. Ying: *Fast multiscale Gaussian wavepacket transforms and multiscale Gaussian beams for the wave equation*, SIAM J. Multiscale Model. Simul. 8 (2010) 1803–1837.

[38] J. Qian, L. Yuan, Y. Liu, S. Luo, R. Burridge: *Babich's expansion and high-order Eulerian asymptotics for point-source Helmholtz equations*, J. Sci. Comput. 67 (2016) 883–908.

[39] S. Serna, J. Qian: *A stopping criterion for higher-order sweeping schemes for static Hamilton-Jacobi equations*, J. Comput. Math. 28 (2010) 552–568.

[40] W. W. Symes, J. Qian: *A slowness matching Eulerian method for multivalued solutions of eikonal equations*, J. Sci. Comput. 19 (2003) 501–526.

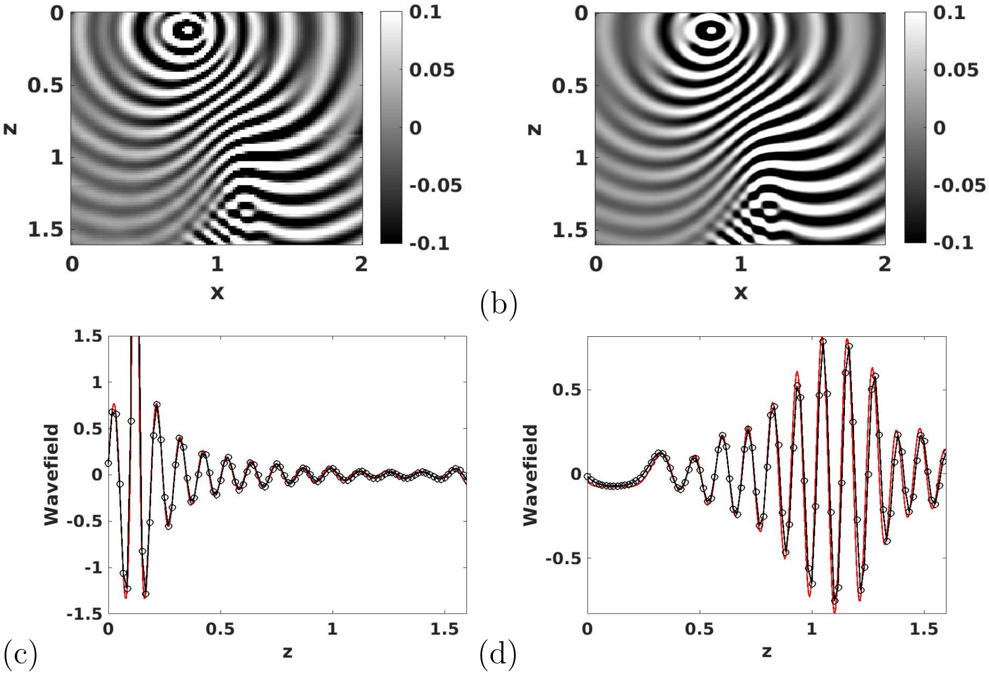

(a) (b)

(c) (d)

Figure 6.1: Example 4 with $\boldsymbol{r}_0 = (0.8, 1.0, 0.12)^T$ and $\omega = 12\pi$. The real part of the xx-component of $\boldsymbol{G}(\boldsymbol{r}; \boldsymbol{r}_0)$ at $y = 1.0$ computed via (a) the Huygens sweeping method with $p = 13$ and (b) the FDTD method.
The detailed comparison of the real part of the xx-component of $\boldsymbol{G}(\boldsymbol{r}; \boldsymbol{r}_0)$ at (c): line $x = 0.8$ and $y = 1.0$ and (d): line $x = 1.2$ and $y = 1.0$. Red solid line: the FDTD solution. Black circled line: the solution of the Huygens sweeping method. Mesh in (a): $121 \times 121 \times 97$; mesh in (b): $401 \times 401 \times 321$.

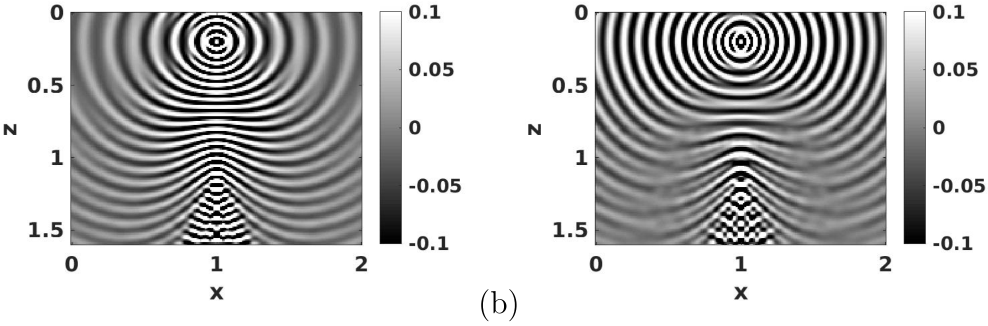

(a) (b)

Figure 6.2: Example 4 with $\boldsymbol{r}_0 = (1.0, 1.0, 0.2)^T$ and $\omega = 20\pi$. The real part of $\boldsymbol{G}(\boldsymbol{r}; \boldsymbol{r}_0)$ at $y = 1.0$ computed by the Huygens sweeping method with $p = 13$: (a) the xx-component and (b) the zz-component. Mesh $201 \times 201 \times 161$.

[41] A. Toflove, S. C. Huganess: *Computational Electrodynamics: the Finite Difference Time Domain Method*, 2nd ed., Artech House, Norwood (2000).

[42] B. S. White: *The stochastic caustic*, SIAM J. Appl. Math. 44 (1984) 127–149.

[43] L. Ying: *Sparse Fourier transform via butterfly algorithm*, SIAM J. Sci. Comput. 31 (2009) 1678–1694.

[44] L. Zhang, J. W. Rector, G. M. Hoversten: *Eikonal solver in the celerity domain*, Geophys. J. Internat. 162 (2005) 1–8.

[45] Y. T. Zhang, H. K. Zhao, J. Qian: *High order fast sweeping methods for static Hamilton-Jacobi equations*, J. Sci. Comput. 29 (2006) 25–56.

[46] H. K. Zhao: *Fast sweeping method for eikonal equations*, Math. Comput. 74 (2005) 603–627.